09

E7.5 10.2.0.5 III

CR-142391

(E75-10205) EVALUATION OF ERTS-1 IMAGE SENSOR SPATIAL RESOLUTION IN PHOTOGRAPHIC FORM Final Report (Arizona Univ., Tucson.) 93 p HC $4.75 CSCL 05B

N75-21730

Unclas
G3/43 00205

Evaluation of ERTS-1 Image Sensor Spatial Resolution in Photographic Form

R. A. Schowengerdt

P. N. Slater

Final Report

Prepared for

NASA/ERTS Contract Number NAS5-21849

Proposal Number 618

Principal Investigator

P. N. Slater (UN237)

1618A

January 1975

Table of Contents

Introduction

The objectives of this program were to:

1) Measure the Optical Transfer Function (OTF)[1] for each band of the ERTS-1 Multi-Spectral Scanner (MSS) from third generation 70 mm photographic products.

2) Determine if any changes occurred in the MSS OTF over a period of several months.

3) Compare the MSS third generation photographic product OTF for one band with the OTF of the corresponding digital image, from a Computer Compatible Tape (CCT).

These objectives were attained by digital Fourier analysis of MSS imagery and simultaneous underflight U2 imagery. Verification of this new technique for OTF calculation was provided by microdensitometer scans of a line target, specifically a long bridge over the San Francisco Bay.

In addition to performing the above tasks, an additional study was made of the MSS imagery, using coherent light Fourier analysis. This study not only produced a multi-band MSS image quality comparison but also a relative comparison in spatial resolution with imagery from the Apollo IX S065 multispectral camera experiment.

The above studies were actually directed to different goals. The OTF is useful for specifying sensor and overall system performance but is only one factor in the quality or information content of given images. On the other hand, Fourier analysis of imagery yields data directly related to its information content, but cannot easily separate contributing factors to the total information in given images. A summary of the results obtained from this program is given in the following section.

[1]The OTF is the spatial frequency response of an optical system (Goodman, 1968). It is a complex function, having both real and imaginary parts, of spatial frequency. Also see footnote on following page.

SECTION I

Introduction and Summary

Author-Identified Significant Results

The following are significant results from the digital OTF measurements made during this program:

1) There are no significant differences in optical performance, in terms of the OTF, among all four bands of the ERTS MSS.
2) There were no substantial changes in the OTF's of bands 4, 5, and 6 during the period November 1972 to May 1973. Imagery from April 1973 did show a slight decrease in the Modulation Transfer Function (MTF).[1]
3) Comparison between the photographic and digital (CCT) two-dimensional OTF's indicated a strong asymmetry in the photographic product OTF between the MSS scan direction and across scan direction. This could be due to D/A data conversion or the Electron Beam Recorder (see Fig. 5 of text).

The following are significant results from the coherent light Fourier analysis conducted during this program:

1) For agricultural areas, bands 5 and 7 of the MSS are superior in terms of image definition, and therefore mapping and acreage estimation.
2) Amplitude modulation in imagery from MSS bands 4 and 5 is between 65-90% of that in corresponding bands of Apollo IX S065 imagery.
3) MSS band 5 imagery has a ground resolution between 55-75% of that exhibited in the corresponding band of Apollo IX S065 imagery.

[1]The MTF is the modulus of the complex function OTF, and is, for most optical systems, nearly equal to the real part of the OTF, the imaginary part being negligibly small. However, throughout this report, the distinction between OTF and MTF is maintained.

LIST OF ILLUSTRATIONS

SECTION II

ERTS-1 MSS System OTF

MEASUREMENT OF THE EARTH RESOURCES TECHNOLOGY SATELLITE (ERTS-1) MULTI-SPECTRAL SCANNER OTF FROM OPERATIONAL IMAGERY

Introduction

Historically, the OTF of aerial systems has been obtained from special targets, such as artificial edges (Roetling, et al, 1969) or lines (Hendeberg and Welander, 1963), or their naturally occurring couterparts in the form of coastlines, field boundaries, etc. The OTF, $\tau(\bar{f})$, can then be obtained directly from the Fourier spectrum, $I(\bar{f})$, of the image by the imaging equation,

$$\tau(\bar{f}) = I(\bar{f})/O(\bar{f}),^{1} \qquad (1)$$

since the object spectrum $O(\bar{f})$ is assumed to be constant [i.e., $o(\bar{x})$ is a Dirac delta function, $\delta(\bar{x})$, for a line target; or effectively a delta function, after differentiating $i(\bar{x})$, in the case of Edge Gradient Analysis (EGA)].

For high ground resolution systems, such as reconnaissance cameras, artificial targets can be of reasonable size, facilitating deployment and maintenance. However, low ground resolution systems, such as the Earth Resources Technology Satellite Multi-Spectral Scanner (ERTS-1 MSS) require prohibitively large targets (e.g., the ERTS instantaneous field of view of 80m x 80m necessitates an edge or line target at least 240-320 m long to apply such techniques as EGA with confidence).

[1] $\bar{f}$ is the spatial frequency vector and is the Fourier conjugate of the spatial vector $\bar{x}$.

Therefore, for low ground resolution sensors, "targets of opportunity" such as bridges or coastlines have to be used. In addition to being under the same size constraints as artificial targets, these objects are generally of unknown quality and may contain detailed structure which introduces error in the OTF calculation.

For these and other reasons (Schowengerdt and Slater, 1974), we have been investigating a different approach, which is particularly applicable to low ground resolution, multi-spectral systems such as the MSS. In our technique, we exploit the substantial ground scale difference between the MSS imagery and imagery from simultaneously flown aircraft underflights (a fairly common practice as an aid in interpretation and discrimination of ground features) to measure $O(\bar{f})$ for an *arbitrary* ground scene. $\tau(\bar{f})$ is then obtained from (1) after determining $I(\bar{f})$ from the orbital imagery.

Details of the technique are discussed in the following sections. A brief outline is given here as an introduction to the concept.

Figure 1 depicts two image formats, one from the spacecraft and one, drawn at the same scale, from the aircraft underflight. Also shown in the underflight image, at its actual size (say both images are 70 mm). Typical combinations of focal lengths and altitudes for the two sensors give scale differences of 7 to 10. Thus the low spatial frequencies in the underflight image are higher spatial frequencies (by the factor 7 to 10) in the spacecraft image. The spacecraft systems of concern here have cutoff frequencies of 30 to 50 cycles/mm and the corresponding underflight spatial frequencies are no greater than 4 to 7 cycles/mm. If the underflight sensor OTF is unknown, it can be reasonably assumed that, at

these low frequencies, the OTF is real and equal to 1, and thus the underflight image is effectively the object for the spacecraft sensor.

To measure $o(\bar{x})$ and $i(\bar{x})$ [and hence $O(\bar{f})$ and $I(\bar{f})$] we do either a single microdensitometer scan (1-D) between two ground reference points in both images or a two-dimensional (2-D) raster scan over the same ground area in both images. In the 1-D scan case a slit-type aperture is used and its length (but not necessarily width) must be scaled as closely as possible to the scale between the images.

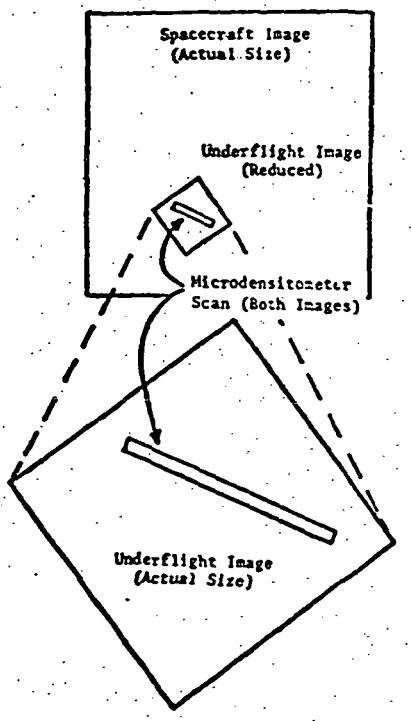

Fig. 1. Geometry of Scaling Technique

The two sets of digitized microdensitometer data are scaled and correlated, subject to some optimization criterion, Fourier transformed, and the spectra ratioed to give $\tau(\bar{f})$. For the 1-D case, under certain conditions (Schowengert and Slater, 1972), we obtain a profile of $\tau(\bar{f})$ for some azimuthal direction. In the 2-D case, we of course obtain the full two-dimensional $\tau(\bar{f})$.

Finally, Fig. 2 is presented to give a convenient visual representation of the scaling concept. In Fig. 2 an ERTS image has been enlarged to be on the same scale as the underflight image, taken by a U2 aircraft at 20 km altitude. The blurring of ground detail in the ERTS image is the result of the spacecraft sensor OTF filtering spatial frequencies appearing in the underflight image.

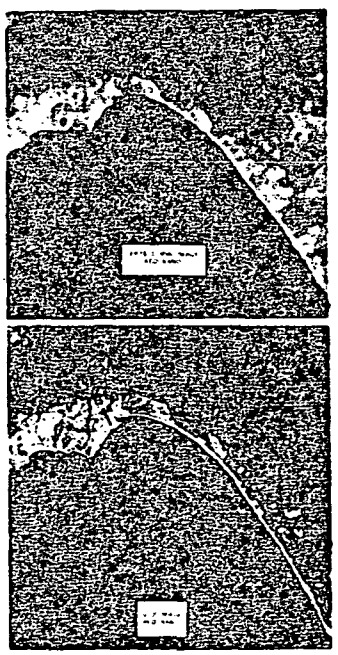

Fig. 2. ERTS-1 MSS and aircraft underflight images (red band) at the same scale.

The ERTS System

It is worthwhile to review the total ERTS imaging system in order to understand its peculiar characteristics and how they are manifested in analysis of the imagery. The ERTS-1 satellite carries two imaging sensors, a set of three Return Beam Vidicon (RBV) cameras, which have not been operated since shortly after launch, and a Multi-Spectral Scanner (MSS). The image is formed in the MSS by a Ritchey-Chrétien system with a focal length of 82 cm, and is swept across a bank of detectors by an oscillating mirror (Fig. 3). The detectors are filtered into four spectral bands (Fig. 4), and there are six adjacent detectors in each band, thus giving six scan lines per band for each cycle of the mirror.

In Fig. 5, the remainder of the image-forming process is depicted. The analog signal from each detector is sampled and the digitized data are either transmitted directly to a receiving station or stored on a magnetic tape for later transmission to earth. The data is then either reformatted to form a Computer Compatible Tape (CCT) or converted back into an analog signal for input to an Electron Beam Recorder (EBR) which produces 70-mm photographic transparencies.

There are various other forms of output products not shown in Fig. 5, such as color composites made from a combination of images from several bands, and scene-corrected imagery which has some residual distortions removed to provide more accurate cartographic data. Our interest is only in the CCT's and third generation 70-mm photographic products, since these are the most widely used images. A typical MSS Photographic image is shown in Fig. 6. The x and y axes referred to in this paper are defined in Fig. 6.

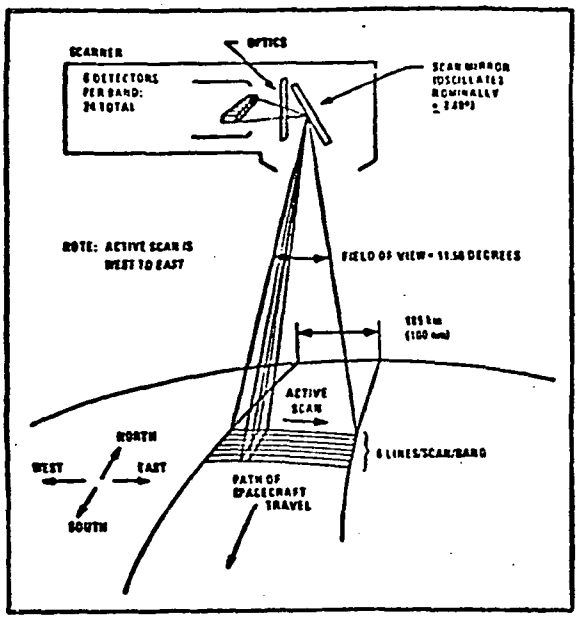

Fig. 3. ERTS-1 MSS Scanning Geometry

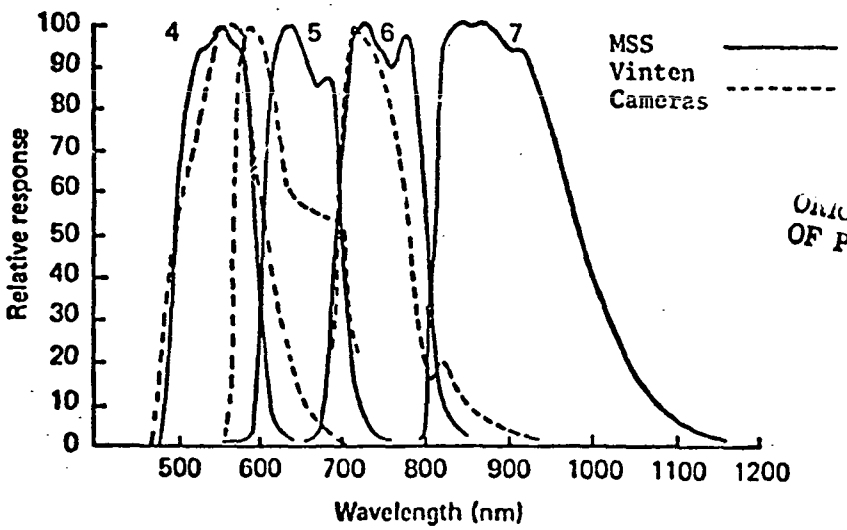

Fig. 4. Spectral Sensitivities of ERTS-1 and U-2 Aircraft Multispectral Sensors

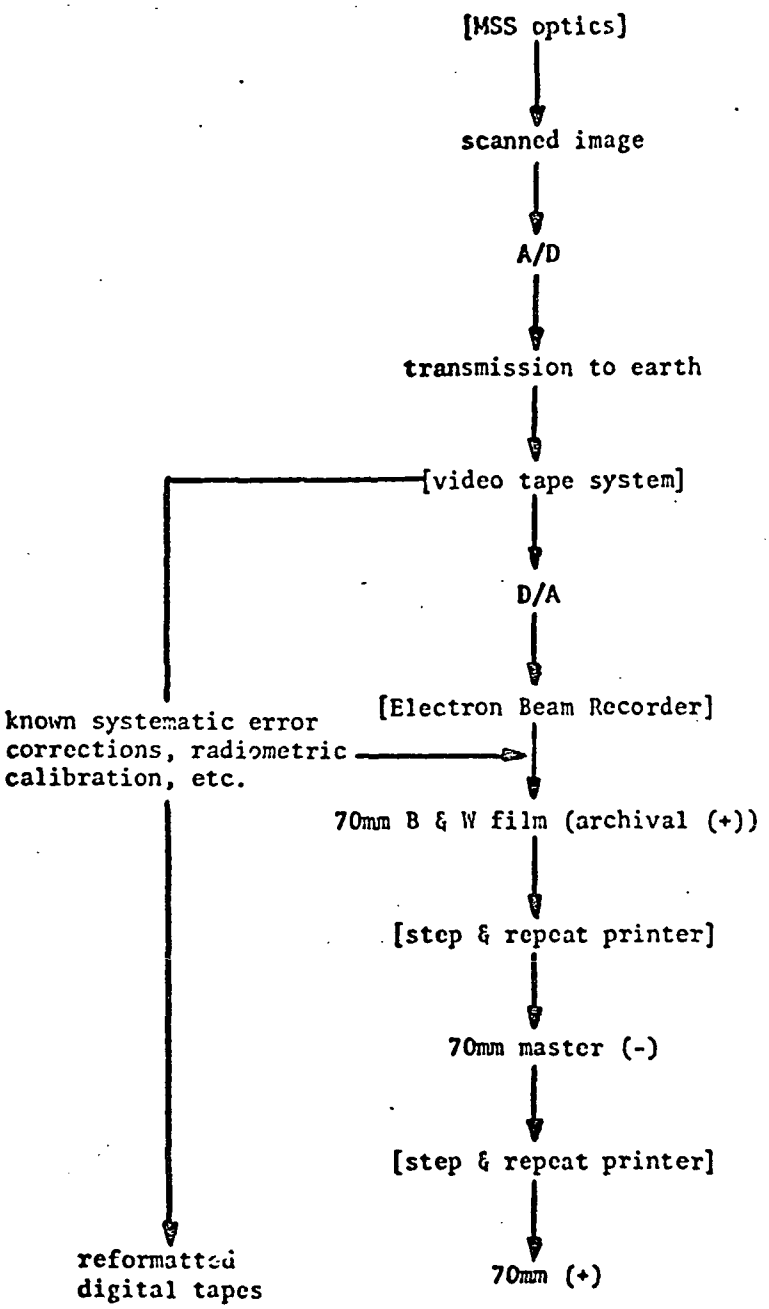

Fig. 5. Data Flow of ERTS-1 System (System Corrected Products)

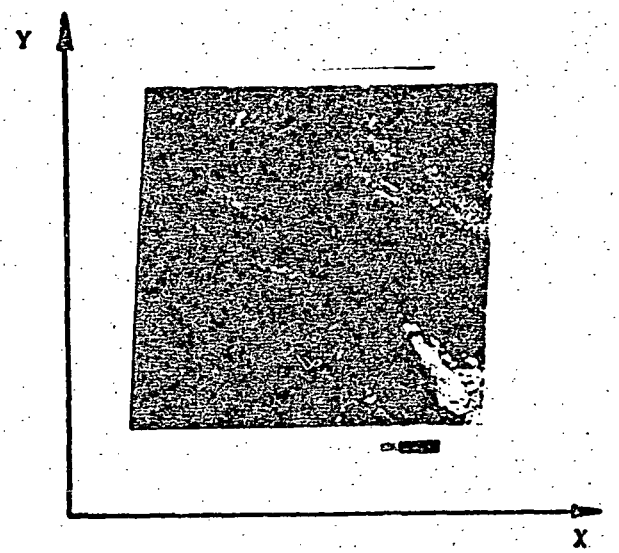

Fig. 6. ERTS-1 photographic image.

Some of the properties of the MSS imagery which are relevant to the application of linear systems theory to measure the overall system OTF are:

1. The geometrical projection of a single detector onto the 70-mm format, is square and about 0.023 mm on a side. Therefore, the 70-mm imagery is band-limited along the x and y axes to approximately 1/0.023 mm, or about, 44 cycles/mm by the finite detector size.

2. The EBR reproduces the analog image signal onto film with an effective focal spot approximately elliptical in shape and with a Gaussian intensity profile. The half-power widths of the spot are 0.007 mm and 0.023 mm, along and perpendicular to the original ERTS scan direction, respectively (Fig. 7). Thus the MSS photographic images are further degraded by the EBR, the degradation being bilaterally symmetric with the x and y axes.

3. A scan anomaly exists in the imagery, particularly in the earlier products. It is most apparent when viewing a long linear structure (such as a bridge) at some angle with respect to the scan direction. The effect converts the linear feature into a staircase shape (Fig. 8, Colvocoresses and McEwen, 1973).

4. In addition to the always present photographic nonlinearities (D-log E curve, adjacency effect, etc.) the output images from the ERTS system are at least third generation duplications. They thus may suffer from contact printing nonlinearities and increased granularity (Jones and Trinks, 1971).

Along ERTS Scan Direction

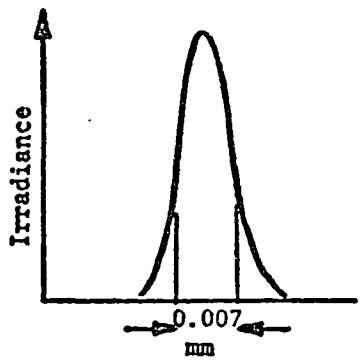

Perpendicular to ERTS Scan Direction

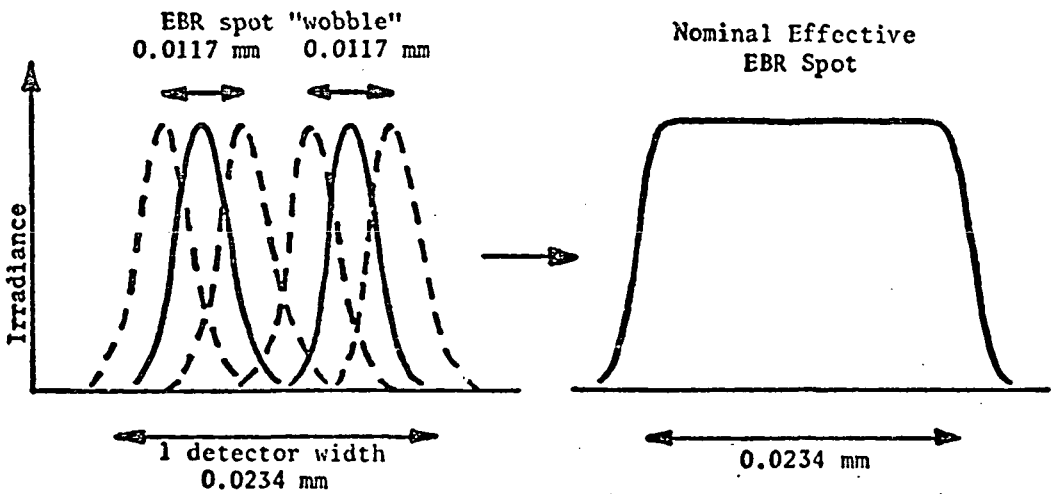

Note: two passes made with EBR spot for each ERTS detector scan

Fig. 7. EBR Spot Geometry

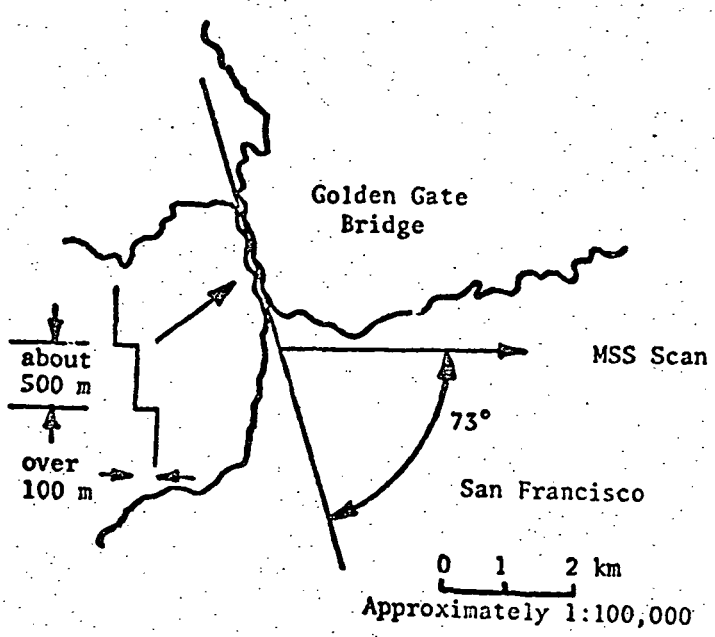

Fig. 8. -- MSS line-scan anomaly (Colvocoresses and McEwen, 1973)

Some of these image properties, such as (3) and (4) above, and others not mentioned here, are not stationary in the sense that their magnitude varies across any given image. On the other hand, (3) might be considered locally stationary for it has no effect on individual image sections, with a y-axis width of less than 0.138 mm resulting from one mirror sweep. In any case, it seems best to qualify any OTF data obtained from this imagery as pertaining only to a particular part of a particular image.

In relation to item (4) above, Fig. 9 (Shaffer, 1973) is a characteristic Modulation Transfer Function (MTF) curve for the ERTS-1 70-mm photographic film/developer combination used in the duplication steps of Fig. 5. The evident nonlinearity around 12 cycles/mm and the dip in modulation transfer below 8 cycles/mm are noted here and discussed in relation to the OTF measurements in following sections of the report.

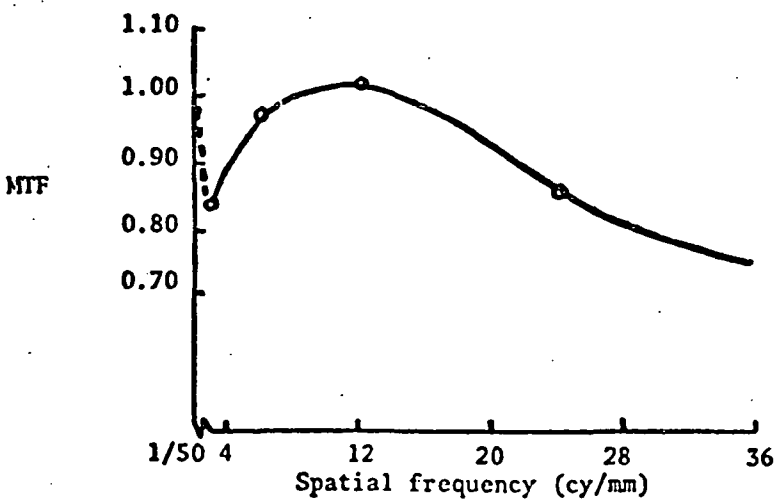

Fig. 9. Typical MTF curve for ERTS-1 film-developer combination (Shaffer, 1973)

Assuming that the EBR process of item (2) above represents a convolution of the EBR spot with the geometrical projection of one detector, we obtain a net spot size of about 0.030 mm. Therefore, the photographic images are band-limited in x and y to about 33 cycles/mm. This limit can be used as *a priori* knowledge of the image to constrain the estimation of point spread functions (PSF) and OTF's from the data as shown in the following sections.

Finally, a brief discussion of the aircraft underflight sensor is in order, since imagery from it is used in the OTF calculation. The aircraft is a U2, flown at 20 km altitude, and the sensor is a set of three 70-mm Vinten cameras with 44.5-mm focal length lenses, filtered as shown in Fig. 4, and loaded with Plus-X and Infrared Aerographic film. The spectral match between this sensor and the MSS is reasonably good, particularly for bands 4 and 6. For our work we receive either second or third generation duplicates of the originals and corresponding step tablets for exposure calibration. For reference, the film-filter combinations for the Vinten cameras are listed below.

A/C Vinten Multispectral Sensor

Band	4	5	6
film	2402	2402	2424
filters	GG-475	OG-570	RG-645
	+	+	+
	BG-18	BG-38	9830

One-Dimensional Approach

It is common microdensitometric practice to use a long scanning slit, whenever possible, to reduce emulsion granularity effects in measuring the modulation of photographic imagery. For this reason, it was decided to try the scaling technique first for the case of a nearly one-dimensional slit scanning a two-dimensional image.

In carrying out the microdensitometric analysis, two small ground features, detectable in both the underflight and ERTS imagery, were used as end points for alignment of the microdensitometer scans. As the length of the scans were typically 30 mm and 4 mm respectively, the angular alignment of the scans could be made accurately.

In order to include the same ground area in each scan of the scan pair, the ratio of the slit lengths should equal the ratio of the scales of the two images. In all the measurements made, it was found that these ratios could be adjusted to be equal within an acceptable 10% error. Since the recorded data along the scan represented a convolution of the aperture with the image, the aperture did not have to be scaled exactly in the scan direction. The data, however, did have to be deconvolved to eliminate the effect of the aperture.

Two conditions have to be met for the analysis to be effectively one-dimensional (Schowengerdt and Slater, 1972). The first is that the length of the scanning slit has to be at least three times the width of the point spread function to be measured. The second is that the contrast of the image at the ends of the scanning aperture has to be low. The first condition was met by suitably adjusting the lengths of the scanning slit and the second condition generally applies because the imagery of a ground

scene from above the atmosphere is usually of low contrast. Table 1 gives typical values for the microdensitometer parameters used in the ERTS analysis. A more detailed table is given in Appendix B.

TABLE 1

TYPICAL MICRODENSITOMETER PARAMETERS

	Slit Length (mm)	Slit Width (mm)	Sample Interval (mm)
U2	.8 - 1.25	.03 - .06	.005 - .010
ERTS	.1 - 0.15	.01 - .02	.005

Figure 10 is a flow chart for a pair of microdensitometer scans (i.e., U2 and ERTS) through the complete OTF calculation. In the data preparation section, the original density values are converted to effective exposure values to which linear systems theory can be applied. The $\cos^4$ (field angle) correction is necessitated in the U2 scan because the scan typically covers a range of 10° to 20° in field angle. (See Appendix D).

The next section of data analysis includes the scaling and spatial shifting of one scan relative to the other to ensure that a conjugate object-image pair of data is analyzed. Since the microdensitometer sampled at whole number multiples of some basic interval and the scale between the images was not generally a whole number, interpolation was required on one set of data to give a one-to-one match between object and image points.

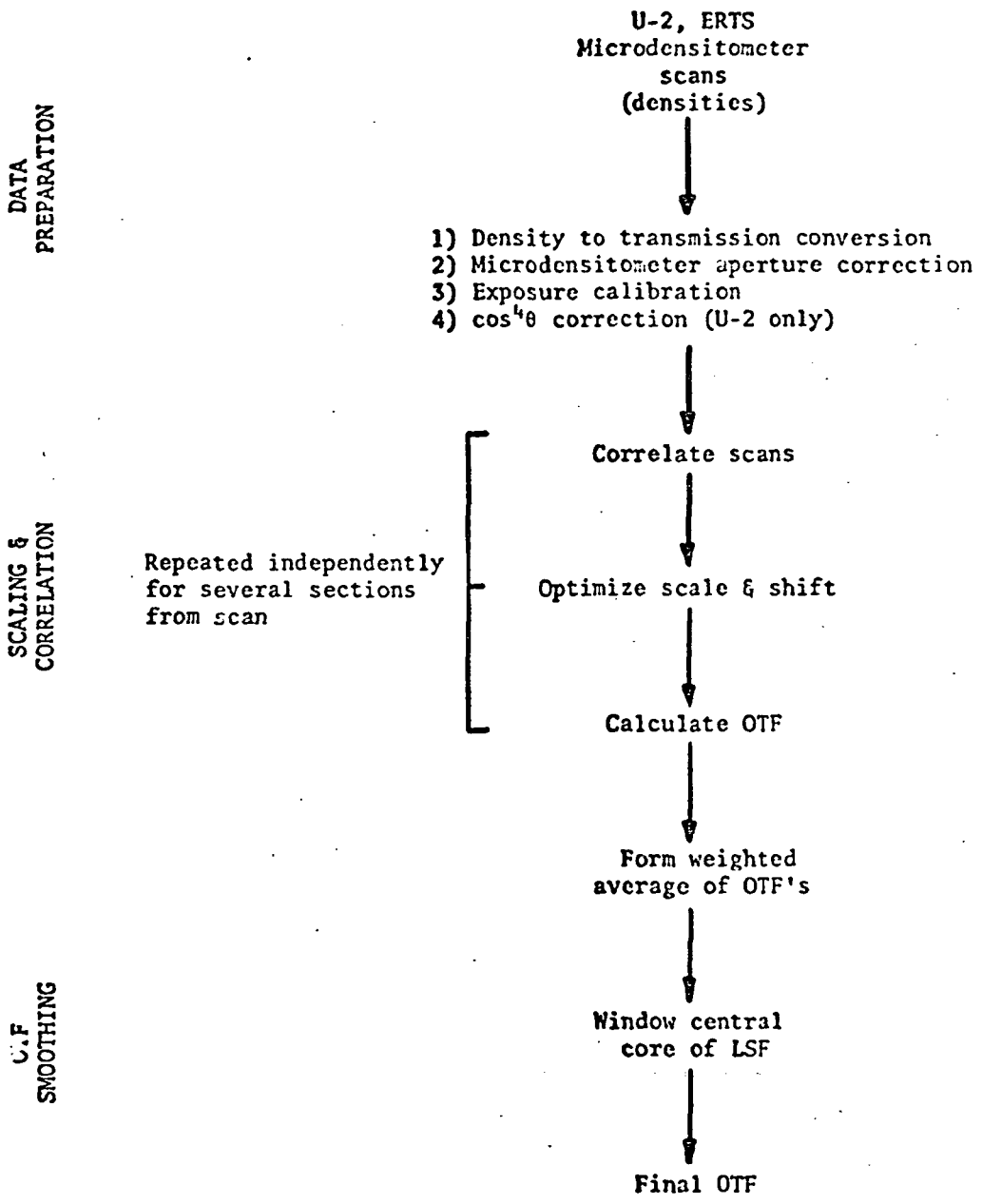

Fig. 10. One-dimensional OTF Analysis

A convenient and exact method for the interpolation of a sampled band-limited function, such as a scanned optical image, is by the convolution of the function with a sinc function (Goodman, 1968, p. 25). The interpolation can be implemented easily in the discrete, Fourier domain by inserting a specified number of zeros between the band-limited, repetitive Fourier spectra (Bergland, 1969). For our application, the U2 data were interpolated by this method. The data were first band-limited sufficiently to allow sampling at an interval of eight times the interval for the ERTS data. The zeros were added, one at a time, between the replicated Fourier spectra, and the spectrum inversely transformed to give a new function, sampled at a slightly smaller interval. In this way, beginning with a data record of 100 points, a change of 1% in the sampled interval was achieved. A more detailed discussion and an example of the interpolation are given in Appendix E.

The scale ratio between the U2 and MSS data was adjusted repeatedly by interpolation on the U2 data, and the new U2 data compared each time with the (unchanged) ERTS data to optimize the scale and spatial shift between the two functions. Care was taken to avoid using data near the end points of the scans because of possible ringing induced by the implied cyclical nature of the interpolation (Bergland, 1969). As an optimization criterion, the fidelity defect, defined as in Eq. 2 by Linfoot (Linfoot, 1964), was found

$$\Phi = \frac{\sum_j [o_j(x) - i_j(x)]^2}{\sum_j o_j^2(x)} \quad , j = \text{sample index} \qquad (2)$$

to be effective in most cases. Figure 11a shows a typical curve of Φ as

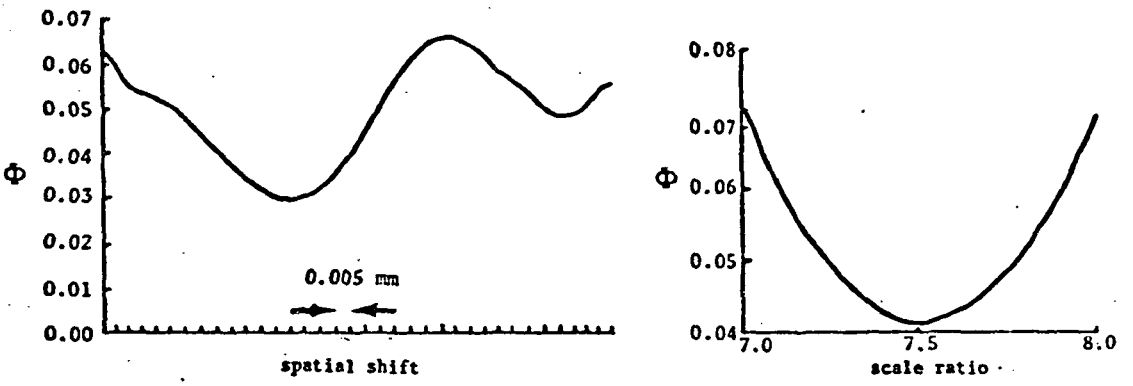

a. Typical spatial correlation at a fixed scale ratio.

b. Typical scale matching

Fig. 11. Matching of ERTS-1 and U2 1-D microdensitometer data.

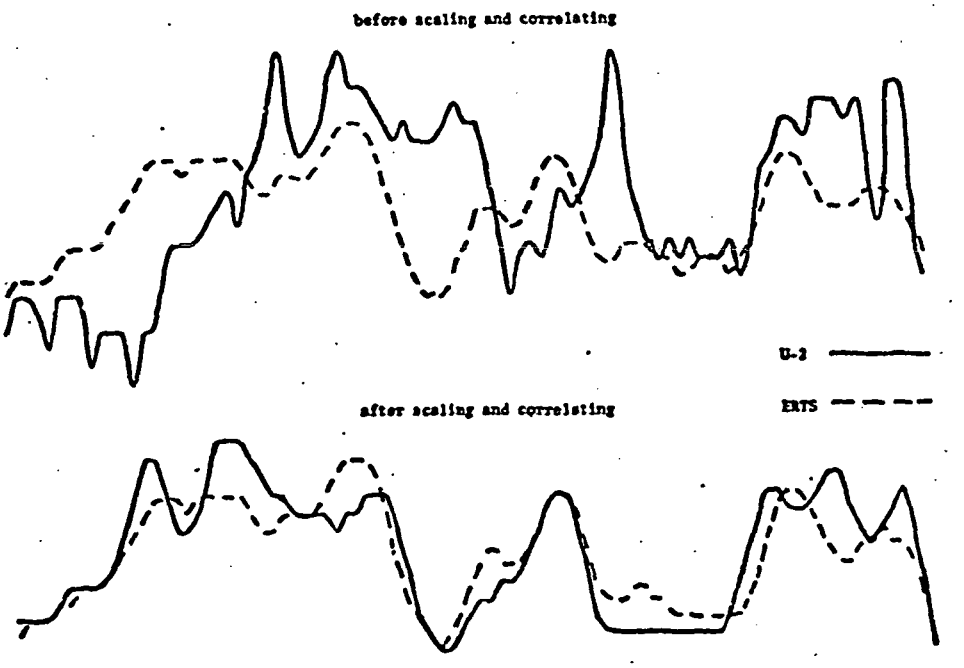

Fig. 12. ERTS-1 and U2 1-D data before and after matching.

o(x) (U2 data) and i(x) (MSS data) are shifted with respect to each other, for a given scale ratio. Figure 11b is formed by plotting the minimum value of Φ from several curves of the type in Fig. 11a, each one corresponding to a different scale ratio between the two images, versus scale ratio.

Figure 12 depicts a typical pair of ERTS and U2 data, before performing the matching process discussed above, and at the optimal match. Some anomalies occur locally in the match e.g., steeper gradients in the image (ERTS-1) compared to the object (U2). However, over the entire region shown, the two scans are matched in terms of their mean squared difference. In addition to possible experimental errors such as scan misalignment, the anomalies may be caused by one or more of the factors discussed in the above section on the ERTS system.

Again because of the cyclical nature of the discrete Fourier transform, each set of data needs to be bracketed with zeros before being Fourier transformed. The number of zeros should be greater than the estimated line spread function (LSF) being measured. However, when this is done, an artificial edge has been generated at each end of the data, which gives rise to erroneously high values for the ERTS OTF. Therefore, an estimate of the ERTS LSF was made using a Gaussian function with a four sigma width equal to the estimated system spot size discussed above. This model LSF was then convolved with the ends of the truncated object scan, and the resulting values used in a weighted average with the measured image values near the truncation, to form a rolled-off edge for the ERTS end sections. The weighted averaging was done to partially account for any error between the estimated and actual ERTS LSF. Figure 13 depicts the correction made to the end points of the ERTS data.

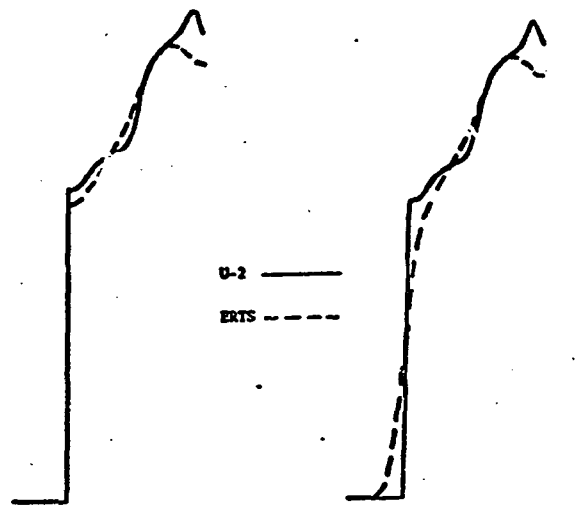

a. data end points before correction.

b. data end points after correction.

Fig. 13. End point correction to ERTS data.

To allow for scale ratio changes along the microdensitometer scan, the data were analyzed independently for each of several sections of the scan. The length of the ERTS data sections was typically 0.5 mm (corresponding to about 3.8 mm on the U2 image). The choice of section length is a compromise between the lowest spatial frequency component measured, given by the reciprocal of the scan length, and the spatial rate of change of scale between the two images. The scale variation appeared to be primarily due to tilt in the non-metric U2 imagery. The number of sections available for analysis, typically 2-4, depends on the length of the microdensitometer scan.

Each pair of matched data were then Fourier transformed and the OTF calculated by Eq. 1. The OTF from each section was then used in a weighted average of the form,

$$\hat{\tau}(\bar{f}) = \frac{\sum_k |O_k(\bar{f})|\tau_k(\bar{f})}{\sum_k |O_k(\bar{f})|}, \quad k = \text{section index} \tag{3}$$

at each frequency, where the weighting function was the modulus of the object spectrum for each section of the scan. Thus the weighting emphasized those values of τ measured from high signal-to-noise ratio frequency components of the object spectrum. Since the average (3) was normalized at each frequency, there was no overall bias introduced in the shape of the average OTF, $\hat{\tau}$.

The OTF's calculated from the ERTS imagery in the above way were found to consistently contain strong harmonic components around 8 to 12 and 30 to 34 cycles/mm. Figure 14 shows a typical unsmoothed MTF curve. The dip below 8 cycles/mm and the high values around 12 cycles/mm are similar to the curve in Fig. 9. The possibility of the correspondence being significant is made more plausible on considering that the images analyzed here are third generation duplications.

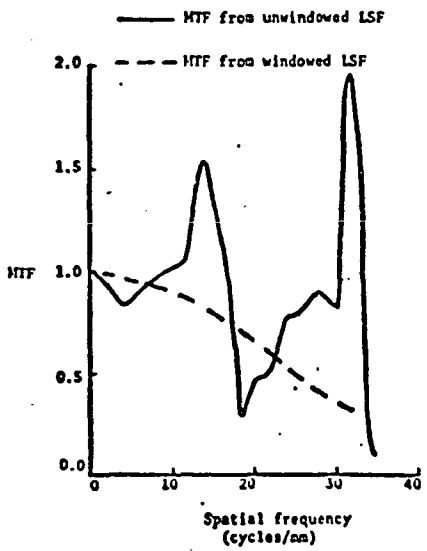

Fig. 14. MTF's from windowed and unwindowed line spread functions.

Transforming the OTF's back to the spatial domain (giving the LSF) allowed for a convenient way to smooth these curves. The harmonics appeared in the LSF as sinusoidal variations superimposed on the LSF core. With a window function[1] (Bergland, 1969, p. 47) applied to the LSF, such that only the core remained, an equivalent smoothing occurred in the frequency domain (Fig. 14). A possible physical interpretation of these results is that the smooth OTF curve represents the linear degradation of the ERTS system and the unsmoothed OTF curve represents both the linear and nonlinear degradation of the system. In addition to this smoothing procedure, the known MSS system spot size at the 70 mm scale of about 0.030 mm, was used to band-limit the ERTS image data and LSF curves. Therefore the noise outside the *a priori* known system band pass was eliminated.

The above procedures were used consistently in obtaining the results presented in the following sections. Although the complex OTF was measured in all cases reported below, usually only the MTF is shown, because the Phase Transfer Function (PTF) was nearly always less than 0.1 spatial cycle. Whenever the PTF is not shown, it is for this reason only.

[1]Windowing is the spatial domain analog of spatial frequency filtering, i.e. multiplication of a function by a smooth truncation type function.

Summary of ERTS Imagery Analyzed

Near simultaneous (within several minutes), cloud free imagery from U2 underflight and ERTS passes was obtained of the San Francisco region on three dates: 11/29/72, 01/04/73, and 04/04/73. The MSS image of 06/15/73 was not available in time for the microdensitometer scans to be made before the end of the program. However, MSS imagery from the previous cycle on 05/15/73 was acquired and analyzed with the U2 imagery from 06/15/73. The only other anomaly in the consistency of data collected was that the U2 imagery from 01/04/73 did not include a green band (4) because of camera malfunction.

Figure 15 shows each ERTS frame which was studied and the microdensitometer scans made of each. The angle between the microdensitometer scan and the MSS scans (x direction) are indicated in Fig. 15. This angle is relevant to OTF data because of possible asymmetries in the spread function introduced by the unequal x-y sampling of the MSS data and the complex EBR spot motion during image reconstruction.

From this microdensitometer data the following scans were analyzed:

Date	Image ID	Scan #	Band
112972	1129-18181	1, 2	4, 5, 6
010473	1165-18173	1	5, 6
040473	1255-18183	2-D array	5
052873	1309-18174	1	4, 5, 6

For the multi-date OTF comparison all of this data is used (with $\theta = -45°$ for 04/04/73). Even though all the θ's are not equal, the total range is only 26°.

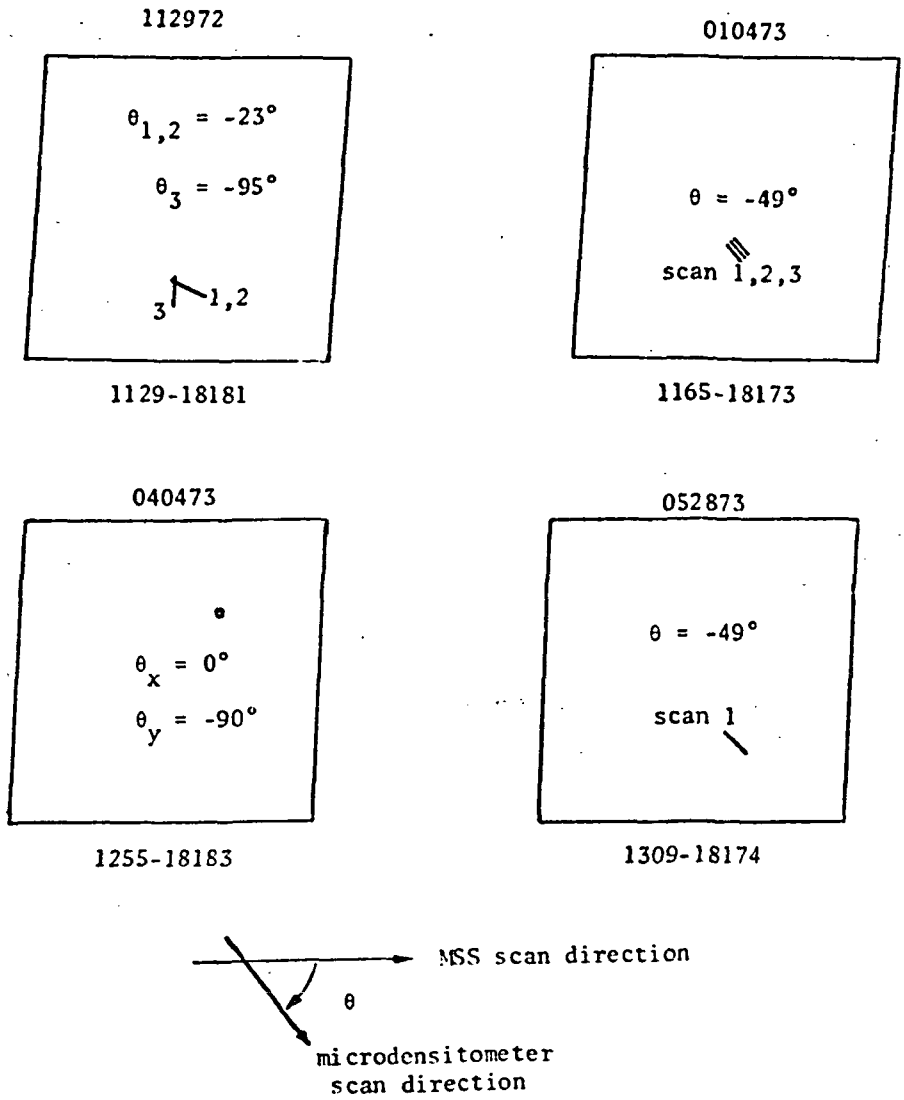

Fig. 15 Geometry of Microdensitometer Scans
ERTS MSS Imagery

Finally, for image #1129-18181, two sets of scans were made with two different aperture sizes (see Appendix B) to determine how critical the choice of slit lengths was to the final OTF obtained. The two OTF's obtained were negligibly different and were averaged in the results reported in the following sections. Details on the two sets of data are given in Appendix E.

Comparison of Scaling Technique to LSF Analysis

A narrow bridge (less than one-third of the ERTS system spot size) in ERTS image #1129-18181 was scanned with a microdensitometer slit. The LSF and corresponding OTF were calculated from the scan and the OTF is compared with the OTF obtained from the scaling technique applied to the same image, see Fig. 16.

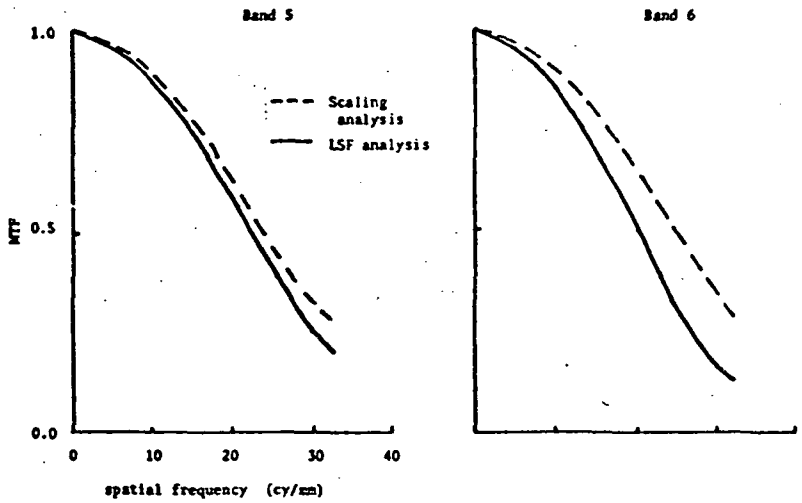

Fig. 16 Comparison of ERTS MSS MTF from scaling technique and from LSF analysis

The orientations of the bridge and scans done for the scaling analysis were such that the LSF and OTF were measured in nearly the same azimuthal direction in both cases. The above figures indicate that the two approaches for measuring the OTF give comparable results, and thus verifies the validity of the scaling technique. The LSF analysis is described in more detail in Appendix C.

Multi-Date MSS OTF Comparison

Figure 17 shows the OTF obtained from several image dates and for the available bands on each date. There appears to be no significant

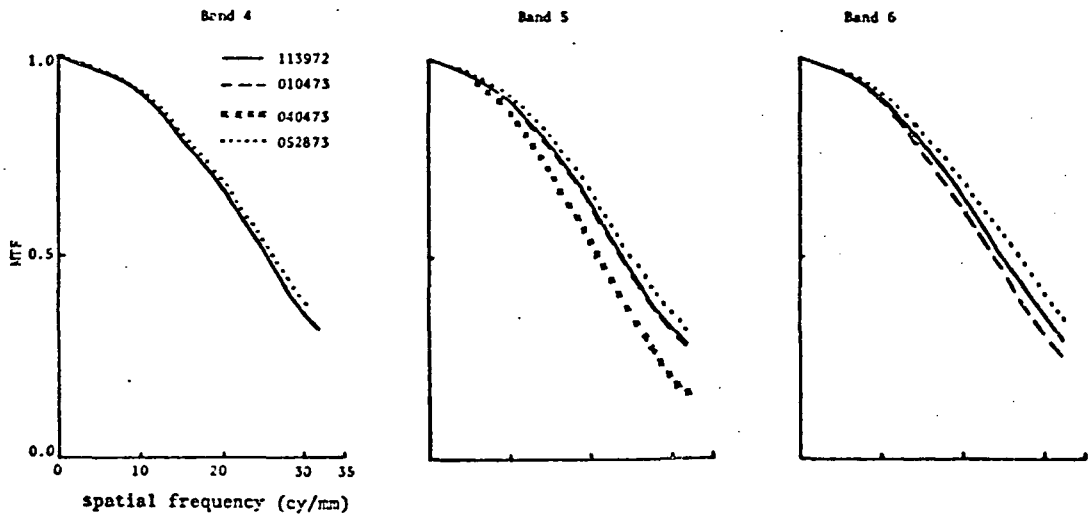

Fig. 17 Mutli-Date ERTS MSS OTF's

changes in the MTF over this time period, except for the small drop for 04/04/73, band 5 (the only band analyzed on that date).

Multi-Band MSS OTF Comparison

In Fig. 18 are shown the OTF's for the available bands of imagery from each of three dates. The curves indicate that there is not any significant difference between the imaging performance of bands 4, 5, and 6 of the ERTS MSS.

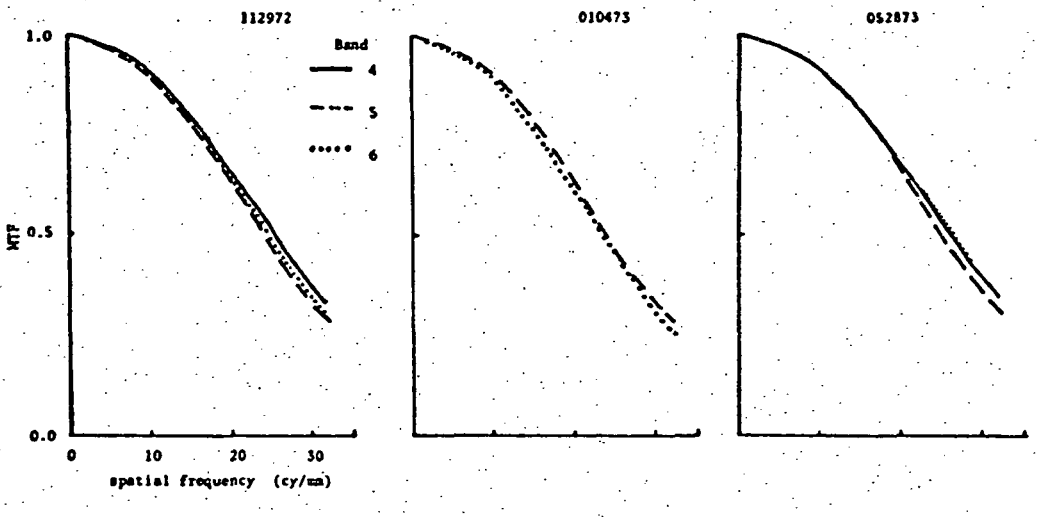

Fig. 18 Multi-band ERTS MSS OTF's for three dates.

Two-Dimensional Approach for Photographic and CCT Images

The 2-D analysis of the spacecraft sensor OTF has several advantages over the 1-D analysis presented above. Some of these are:

1. The two images (underflight and spacecraft) can be scaled and correlated in both the x and y directions.

2. The necessity of scaling the ratio of slit lengths is eliminated.

3. The CCT image data is most conveniently used in its inherent 2-D sampled form.

For the application of 2-D analysis, an area containing high frequency content in several directions was selected from the underflight, ERTS 70-mm photographic image, and ERTS digital CCT image. The images were matched in scale and spatial shift in x and y using Φ as the optimization criterion. Scaling was done, in this case, by spatial polynomial interpolation. The scheme for interpolating the 1-D data was felt to be too slow, computationally, for the 2-D data.

Figure 19 shows the matched images. The loss in ground resolution for the ERTS imagery is again apparent (Fig. 2) as is the noisy character of the photographic image relative to the CCT image. Using analysis analagous to

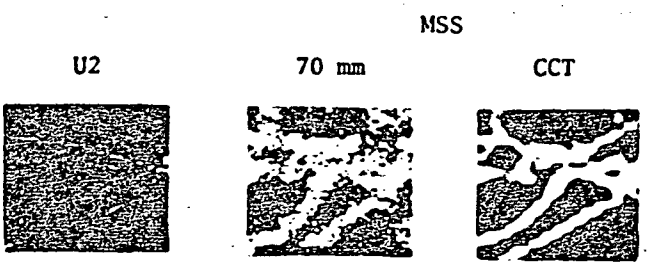

Fig. 19 Scaled and Matched Imagery from 04/04/73, band 5

that for the 1-D case the OTF's and PSF's were calculated for the two ERTS products. As in the 1-D case, the OTF's obtained by the division of the image spectrum by the object spectrum were band-limited at 35 cycles/mm by a circular filter and inverse transformed. The PSF's were then windowed by a circular window analagous to the 1-D window (p. 24) and transformed to yield the final OTF's. Figure 20 shows the OTF profiles

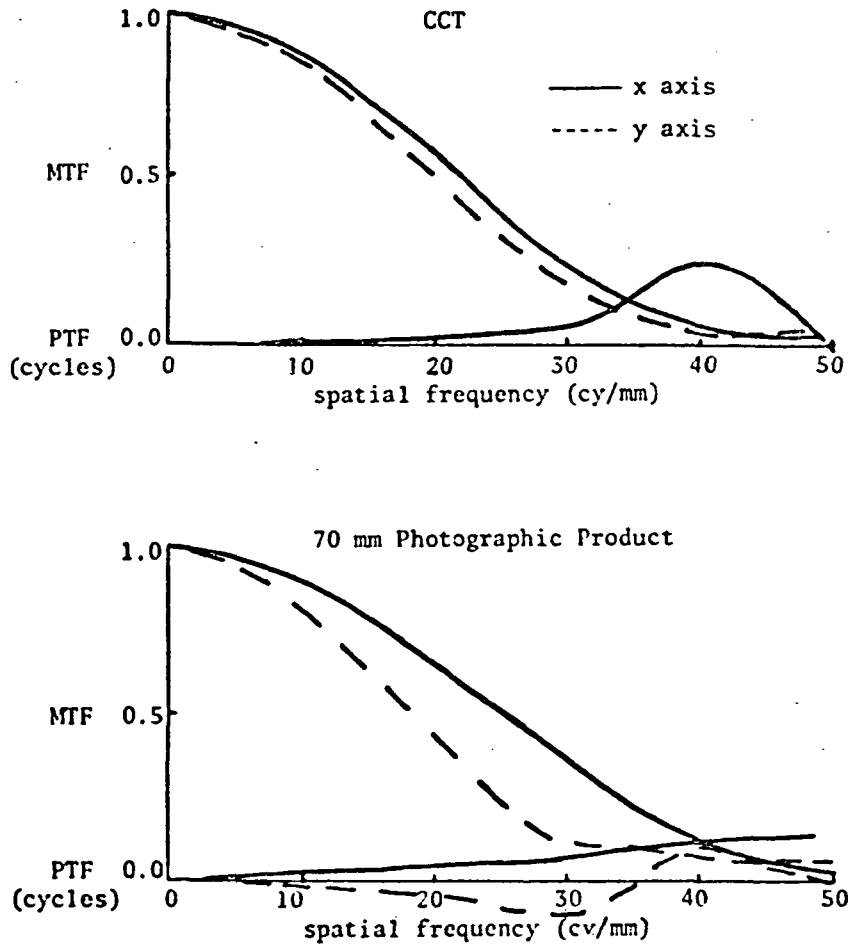

Fig. 20 Two profiles through two-dimensional OTF's obtained for 04/04/73 imagery, band 5

parallel and perpendicular to the ERTS scan direction (along x). The improvement in the MTF for the photographic product versus the CCT OTF, parellel to the scan direction, is probably associated with the nonlinearities of contact printing, photographic processing, etc. In the direction perpendicular to the scan direction, the photographic image MTF shows a substantial decrease from the digital image MTF. A possible explanation for this could be associated with the complex EBR image reproduction process (Fig. 7).

Since the 04/04/73 photographic OTF, along the -45° azimuth, is lower than the OTF's from other dates (see Multi-Date MSS OTF comparison) some effort was spent to determine any inherent differences in the calculation of the OTF's for 1-D data and 2-D data. The results are discussed in Appendix E.

SECTION III

Coherent Optical Fourier Analysis

Introduction

Optical Fourier analysis (Goodman, 1968, Chap. 5) has been used to obtain relative comparisons between ERTS-1 bands 4 and 5 and the Apollo 9 S065 experiment's bands BB and DD. The optical bench arrangement used is shown below.

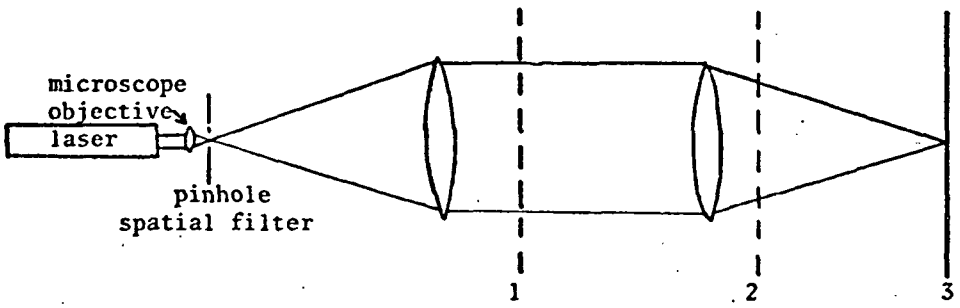

Fig. 21 Optical Fourier Transform Set-up

If a photographic transparency is placed in plane 1, the Fourier transform of the transparency will appear in plane 3. Since the above system is using coherent light, the Fourier transform is performed on the complex amplitude transmission of the transparency. For a transparency with no phase relief or scratches, the amplitude transmission is real (i.e. not complex) and is the square root of the intensity transmission.

Thus, if the transparency has an amplitude transmission given by $t(x_1,y_1)$, the distribution of light in plane 3 is,

$$E_3(x_3,y_3) \propto |\tilde{t}|^2 \propto |FT[t(x_1,y_1)]|^2 \qquad \text{(scaling ignored)} \qquad (4)$$

where FT denotes the Fourier transform. By placing the transparency in plane 2 the scale of the Fourier transform can be adjusted by moving plane 2 relative to plane 3.

Note that the spatial frequency spectrum obtained above is not identical to that obtained by, say, Fourier transforming digital microdensitometer data. In that case, one is transforming the intensity transmission, T, of the transparency,

$$\tilde{T} = FT[T(x,y)]$$
$$= FT[t^2(x,y)] \qquad (5)$$

Generally, (4) and (5) are two distinct functions and one cannot be obtained from the other.

Comparison Between ERTS-1 and Apollo 9 Imagery

A frame was selected from each set of imagery such that the ERTS and Apollo 9 coverage overlapped. The ERTS frame is diagrammed in Fig. 22, the circular area being the region which was transformed. Scaling was performed on the ERTS images to make the ground spatial frequency correspond to the Apollo 9 scale. Prints of the spectra obtained are shown in Fig. 23. The following points can be deduced immediately from Fig. 23:

1) The spikes, denoted A-A', in all cases are due to scratches on the film.
2) The spikes and dots, denoted B-B', in the ERTS spectra are due to lines, caused by faulty calibration of one detector, present in the MSS images. Further discussion of this anomaly is given in Appendix E.
3) The dots, denoted by arrows marked 0 and 1, are due to the periodic square-wave nature of the agricultural fields indicated in Fig. 22. These dots can also be detected in the original photographs of the ERTS spectra at an angle of about 10° to the scan line spikes.

Fig. 24 shows microdensitometer scans of the original spectra transparencies along the azimuthal direction discussed in (3) above. The spectrum in each case was averaged about the origin to obtain these curves.

The data in Figs. 23 and 24 contain the experimental artifact of conversion from exposure to density in the step of photographically recording the spectra. The densities at selected frequencies were converted to relative exposures by using the D-log E curve for the processing of the spectra photography. The amplitude transmission modulation of the original image was then calculated at each frequency by the equation,

$$m_a(f) = \sqrt{E(f)/T_o} \qquad (6)$$

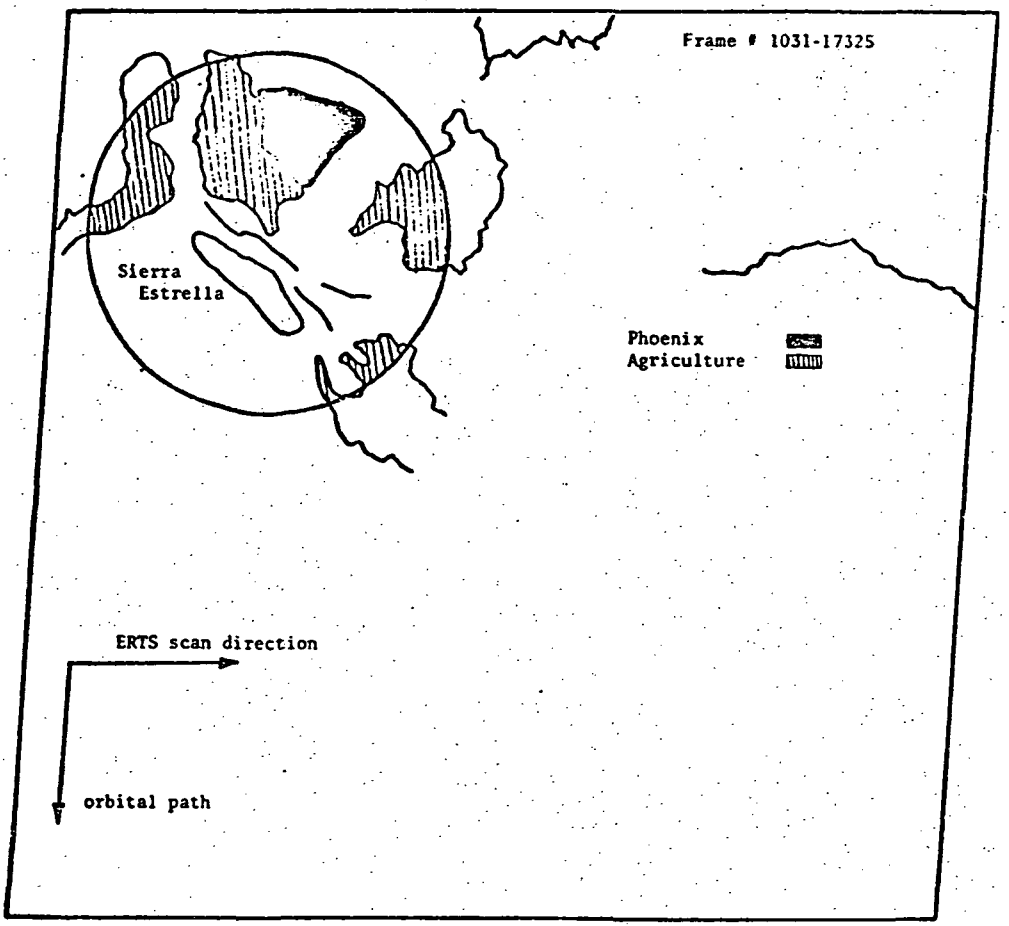

Fig. 22 Diagram of ERTS frame used in optical Fourier analysis experiment. The circled area was Fourier transformed.

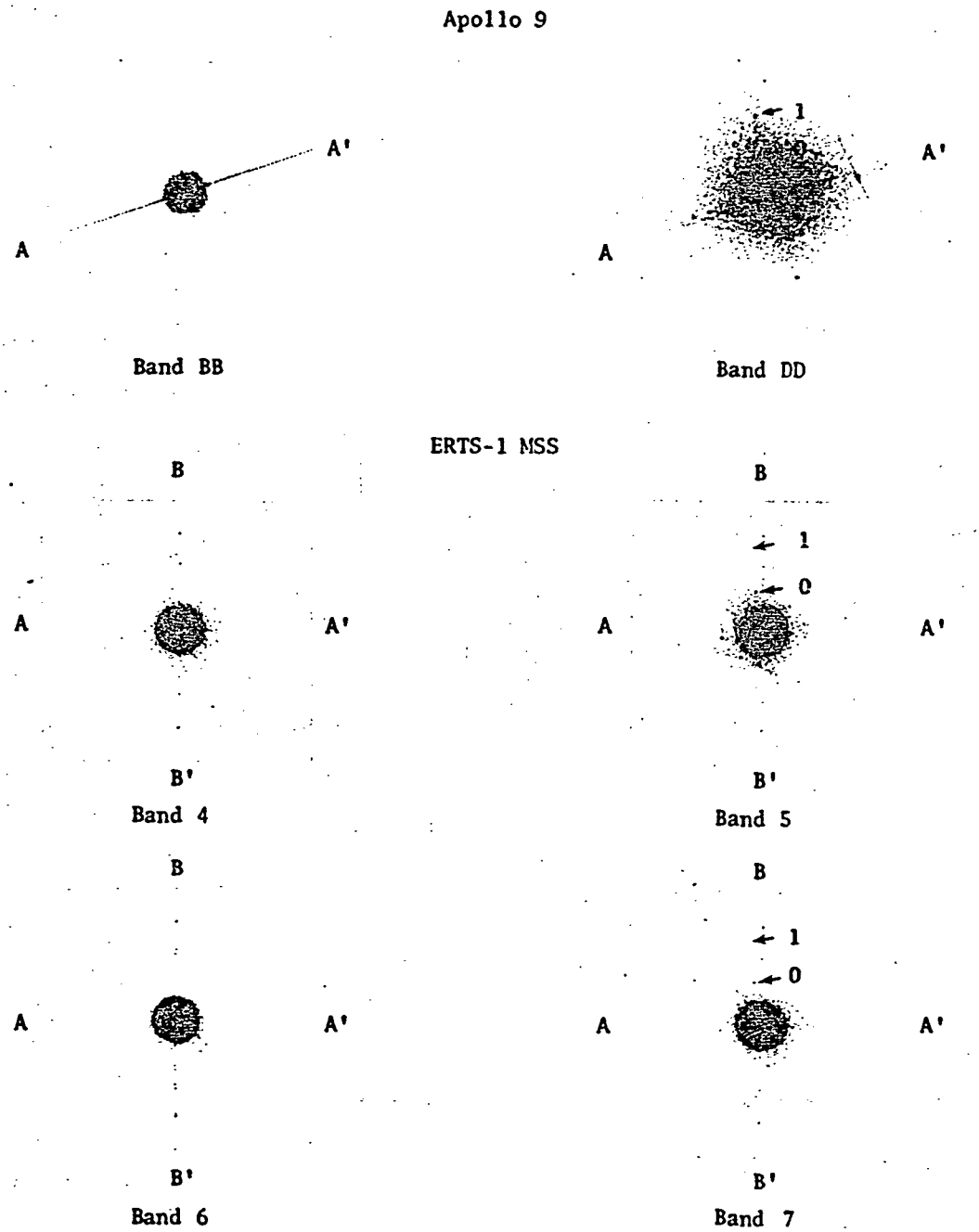

Fig. 23 Prints of the Fourier spectra obtained from the image in Figure 1 and the corresponding Apollo 9 image.

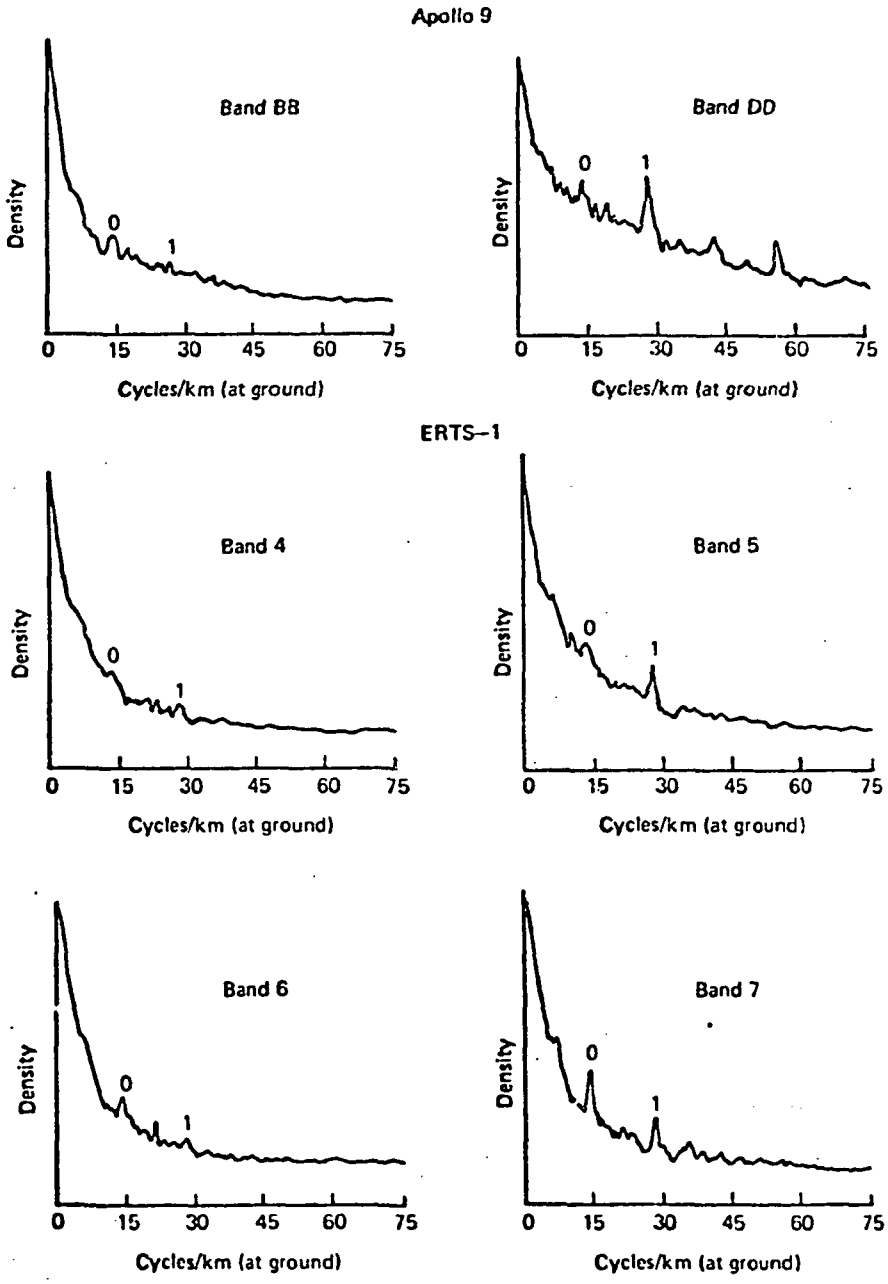

Fig. 24 Microdensitometer scans along a selected azimuth of the photographically recorded Fourier spectra.

where E is the relative exposure in the spectrum at the given frequency and T_o is the average intensity transmission of the area (indicated in Fig. 23) transformed. This formulation was based in the following model. Assume the transparency has an amplitude transmission given by,

$$t(x) = t_o + a_1 \cos 2\pi f_1 x$$

The amplitude transmission modulation is then,

$$m_a = 2a_1/t_o$$

The Fourier transform is taken optically to obtain,

$$\tilde{t}(f) = t_o\delta(f) + \frac{a_1}{2}\delta(f\pm f_1)$$

The intensity is recorded to give,

$$E(f) = |\tilde{t}(f)|^2 = t_o^2\delta(f) + \frac{a_1^2}{4}\delta(f\pm f_1)$$

Since, assuming no phase effects in the image,

$$T_o = t_o^2$$

we have eq. (6)

The resulting curves are shown in Fig. 25. They indicate a true reduction in spatial frequency content between the Apollo 9, band DD, and ERTS-1, band 5. Apollo 9, band BB, and ERTS-1, band 4, are more similar in spatial frequency content, indicating that this band may be limited in resolution by modulation reduction from atmospheric scattering, (or in this case, by the scene modulation in the green) rather than by sensor resolution or data processing.

A number closely related to the ratio of resolution between the ERTS and Apollo 9 sensors can be obtained in the following way. It is reasonable to assume that the spatial frequency at the resolution limit will have a fixed

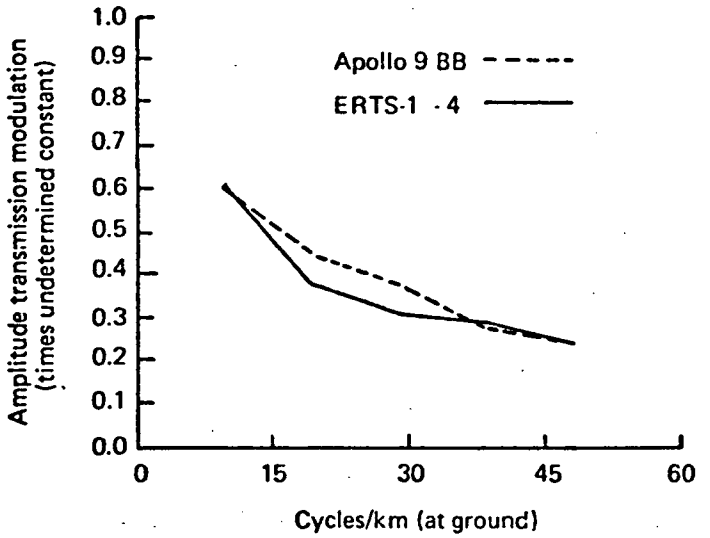

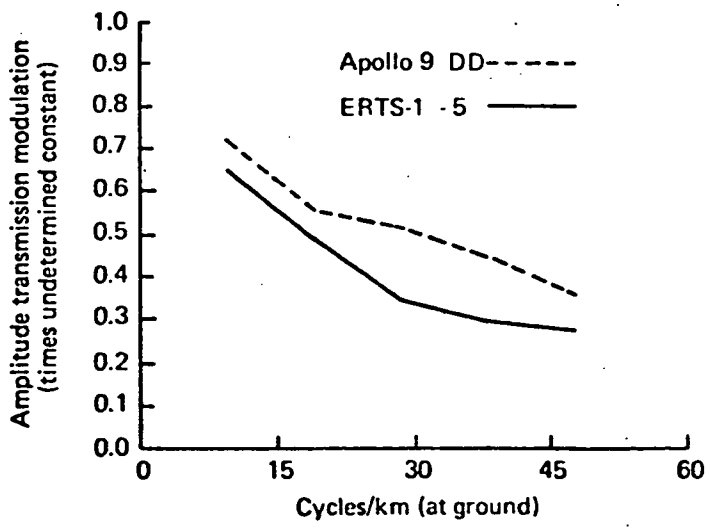

Fig. 25 Amplitude transmission Fourier spectra.

modulation, independent of the particular image. Therefore, lines of constant modulation were drawn on Fig. 25, and the spatial frequency at which they crossed the ERTS and Apollo 9 spectra, were noted. The ratio of frequencies, for the same modulation, between the two images is plotted in Fig. 26. From these curves one can say there is a reduction in ground resolution (defined in this way) from Apollo 9 S065 to ERTS of 0.8 ± 0.1 for the green band and 0.65 ± 0.1 for the red band.

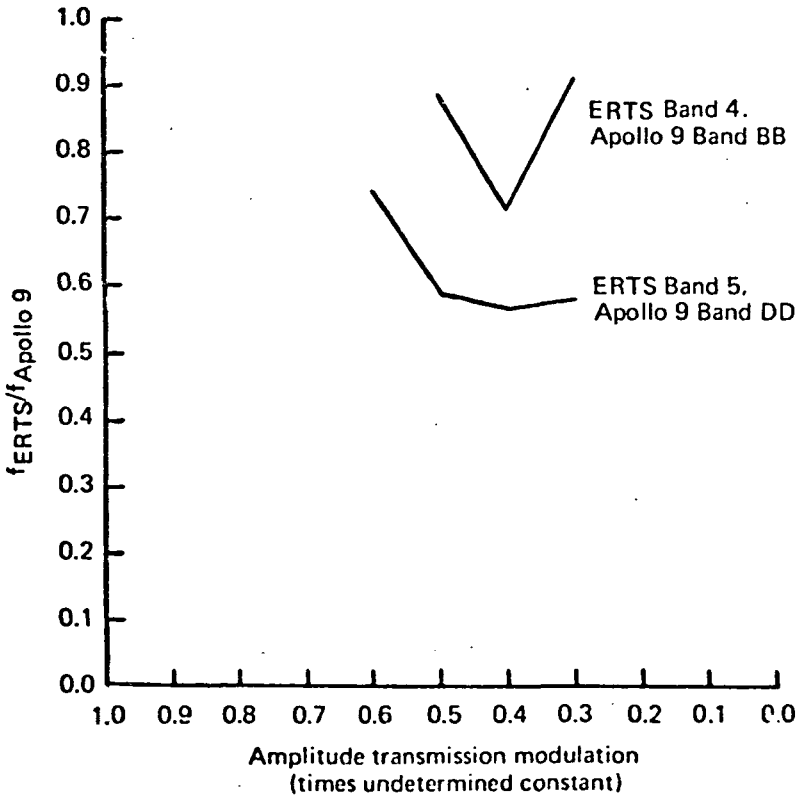

Fig. 26 Ratio of spatial frequencies that have the same modulation in the ERTS and Apollo 9 S065 experiment images.

The following qualifications apply to comparisons between the ERTS-1 and Apollo 9 imagery:

1) The spectral bands are not identical.

2) The imagery was taken at different times of day and 3 1/2 years apart.

3) The imagery examined are only single examples, subject to particular exposure and processing conditions.

Nevertheless, the comparisons are useful in establishing a base line for image information content.

Multi-Band MSS Comparison

Two microdensitometer scans were made for this comparison. One is the data obtained above and is shown, for all ERTS bands, in Fig. 27. Again the amplitude transmission modulation is plotted versus spatial frequency. The red band (5) shows the highest spatial frequency content.

A more discriminating comparison was obtained by calculating the modulation corresponding to the frequency components of the agricultural field patterns (see point 3, p. 36). These components are labeled in Fig.24 as 0 and 1, i.e. the fundamental and 1st harmonic. Fig. 28 is a comparison of the modulations obtained. The strength or modulation of these components indicate the contrast, edge sharpness, and degree of periodicity in the field patterns. It is obvious that bands 5 and 7 are superior, implying that better discrimination between fields could be made with these bands, than with bands 4 and 6.

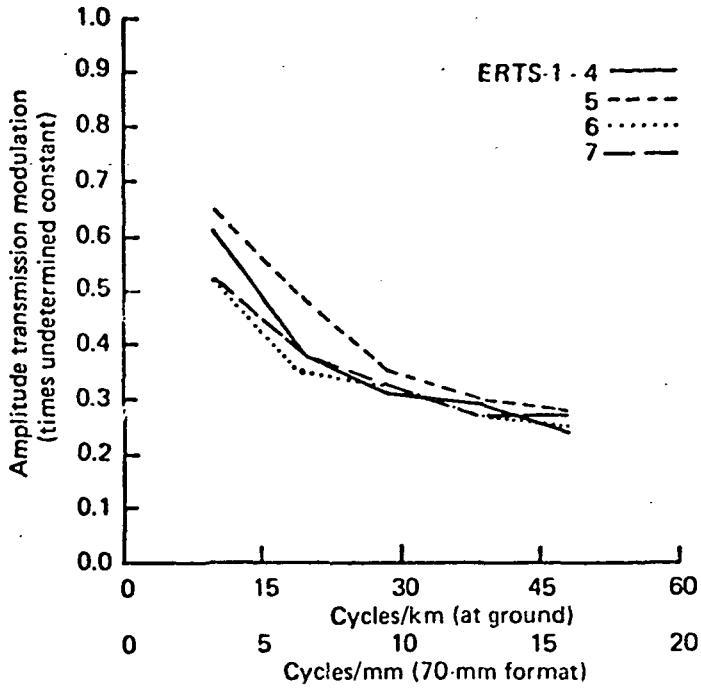

Fig. 27 Amplitude transmission Fourier spectra.

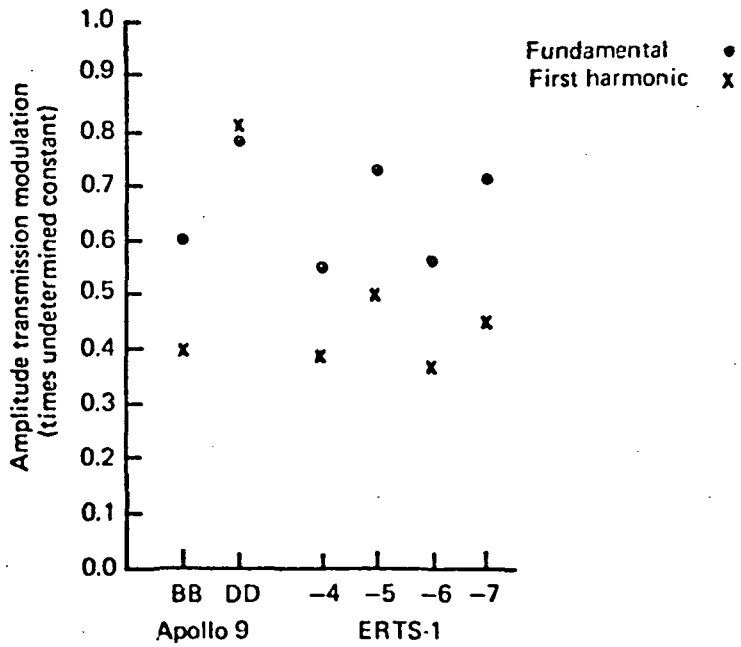

Fig. 28 Modulation at two selected spatial frequencies in the ERTS and Apollo 9 S065 experiment images.

APPENDIX A

Sensitometry and Noise Measurements

Density Calibration of Microdensitometer

The specular density measured by a microdensitometer is generally different than the diffuse density. The ratio of specular to diffuse densities is defined as the Callier Q factor and is always greater than or equal to 1. Q depends on the film type, mean density level, and the microdensitometer optical geometry (specifically the numerical apertures of the influx and efflux optics). To facilitate calibration in this situation the microdensitometer electronics can be adjusted to give readings corresponding to diffuse densities of a step tablet made on material identical to the film used for the imagery. If the Callier Q factor is constant over the given density range, this calibration procedure amounts to multiplying the microdensitometer specular densities by a constant (≤ 1) to give the equivalent diffuse densities.

In practice, the instrument was calibrated in this way for a low and high density step in the given step tablet. Figure 1 shows the calibration for some specific data. It is seen that Callier's Q is nearly constant over the density range, particularly for the A/C film and large microdensitometer slit combination. The microdensitometer densities, being very linear with diffuse densities, permit direct use of the D-log E curve film calibration (excluding adjacency effects) for the microdensitometer readings.

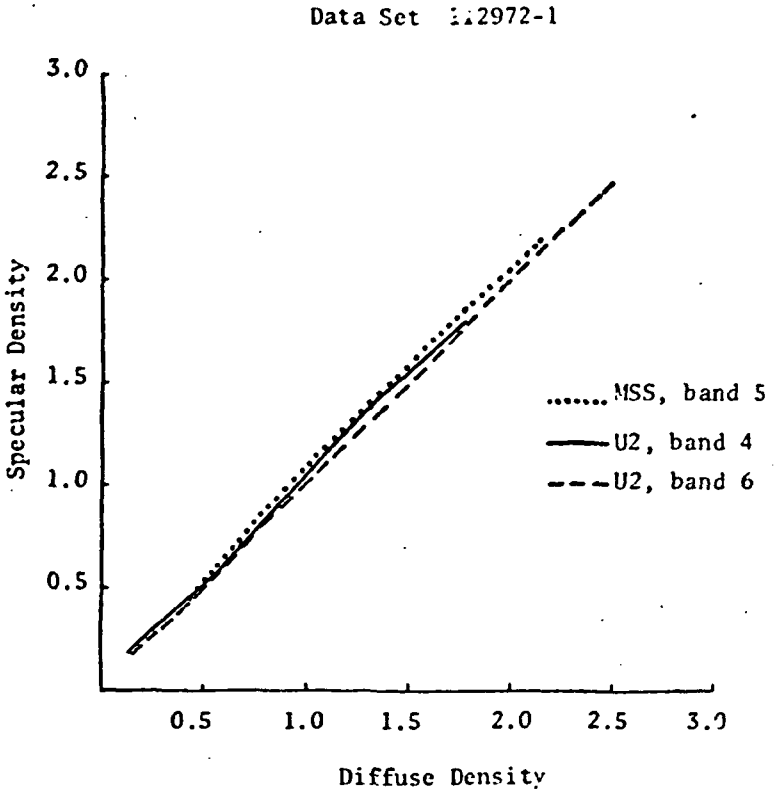

Fig. 29 Microdensitometer Calibration

Rejection of Bad Data Points

An automatic computer algorithm has been written to replace bad points (from pinholes, spots, etc.) in the step tablet scans. After a first-look at the data histograms a rejection threshold about the mean of ±10% of the mean was chosen as a criterion for replacement. The program models the raw histogram (including bad points) with a Gaussian probability density function of the same mean and variance, and generates random numbers from this pdf to replace any points outside the rejection threshold. The new mean (slightly changed from the original) and new variance (substantially reduced from the original) are calculated and the data, with replacement points, is checked for rejection again. If any bad points are found the process is repeated. When all points are "good" the program replaces once more all bad points found in all interations with random numbers generated from a Gaussian pdf with the most recently calculated mean and variance. Thus it converges on the proper mean and variance. Schematically, the process is,

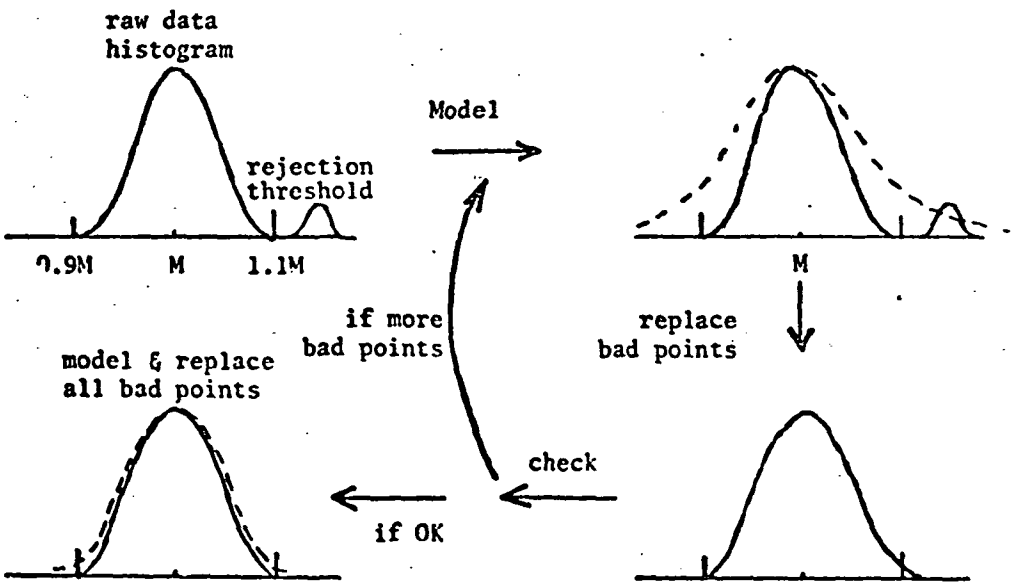

On initial runs of the program, it was found that usually only one iteration was necessary to correct the bad data. The number of bad points in a record was normally less than 5% of the total number of points.

Sensitometry

The Fourier theory of image formation with incoherent light is derived in terms of scene radiance and image irradiance. These two quantities are to be measured from the U-2 underflight image and ERTS-1 image, respectively. Since absolute calibration is impossible for all practical purposes, relative exposures are used which differ from the absolute exposures by at most a mutliplicative constant. The relative exposure is measured from step tablets exposed onto the film of interest.

The step tablet used for the U-2 film is a 21-step tablet filtered similarly to the imagery. It is assumed in generating the exposure points for these data that the original tablet is standard (density range = 0.05 - 3.05) and has a density increment of 0.15 between steps. The exposure for each step is then assumed proportional to the transmission of the original tablet at that step. The effective exposure bias for each particular tablet is taken from the D_{min} + 0.005 point (for a negative) on the curve and is subtracted from all exposure values to give a calibration starting at zero exposure.

The step tablet for the ERTS film is generated during the Electron Beam Recorder (EBR) writing of the original film image. The steps range between 0.0 and 63.0 exposure units in equal increments of 4.5 exposure units. The tablet is duplicated simultaneously with the imagery during later copying steps.

Linear interpolation between step tablet steps was used to calibrate image points. For the ERTS imagery the calibration was done from transmission to effective exposure because the ERTS film processing is controlled to give a nearly linear T versus E curve. For the underflight imagery it was found that, for the range of density values occurring in the images, linear interpolation of the D versus E curve was usually satisfactory. Figures 30 and 31 show the calibration curves used for all the imagery analyzed. The maximum, minimum, and mean exposure values for particular imagery analyzed are shown on the curves.

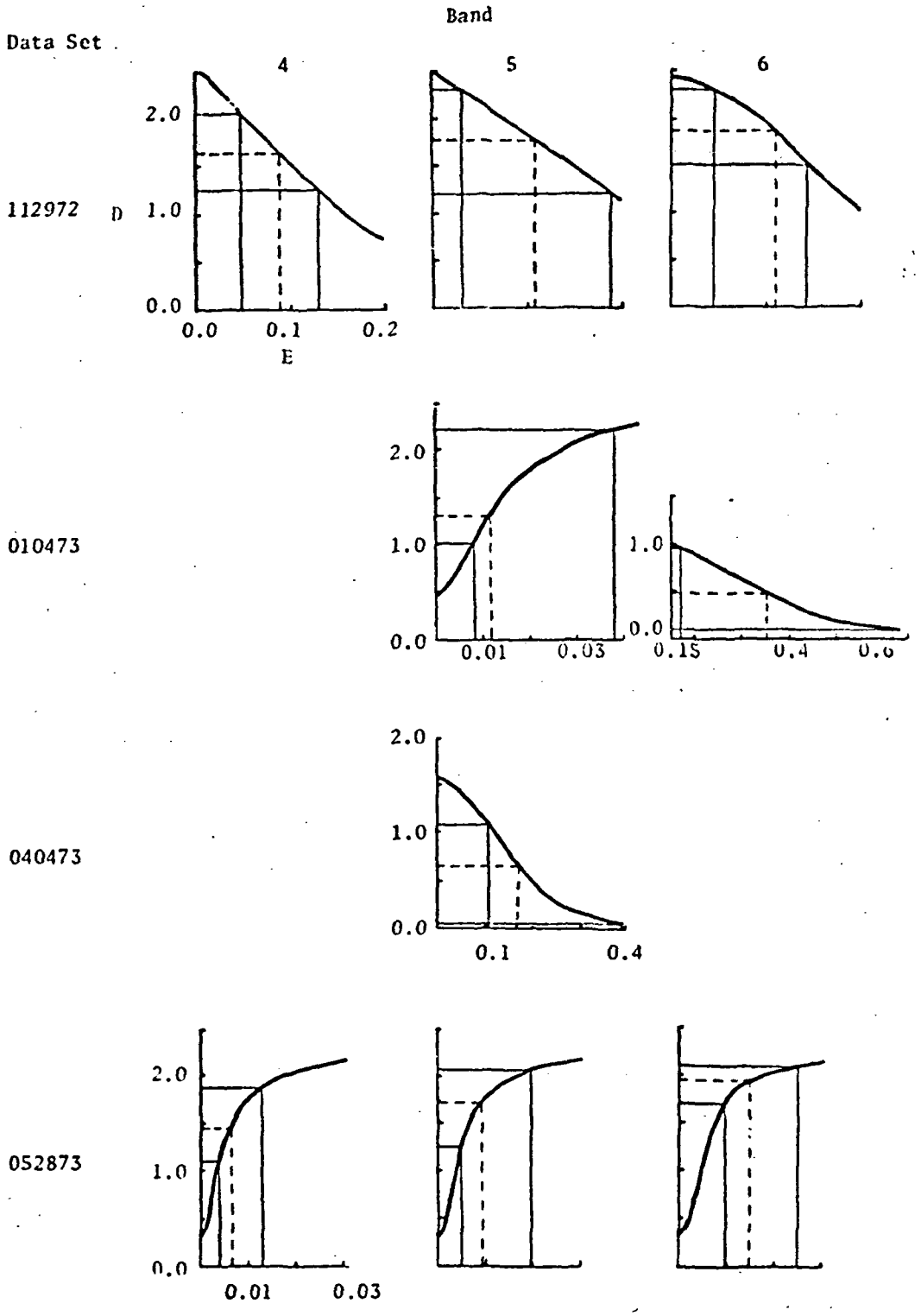

Fig. 30 Underflight Imagery Sensitometry
Density versus Exposure

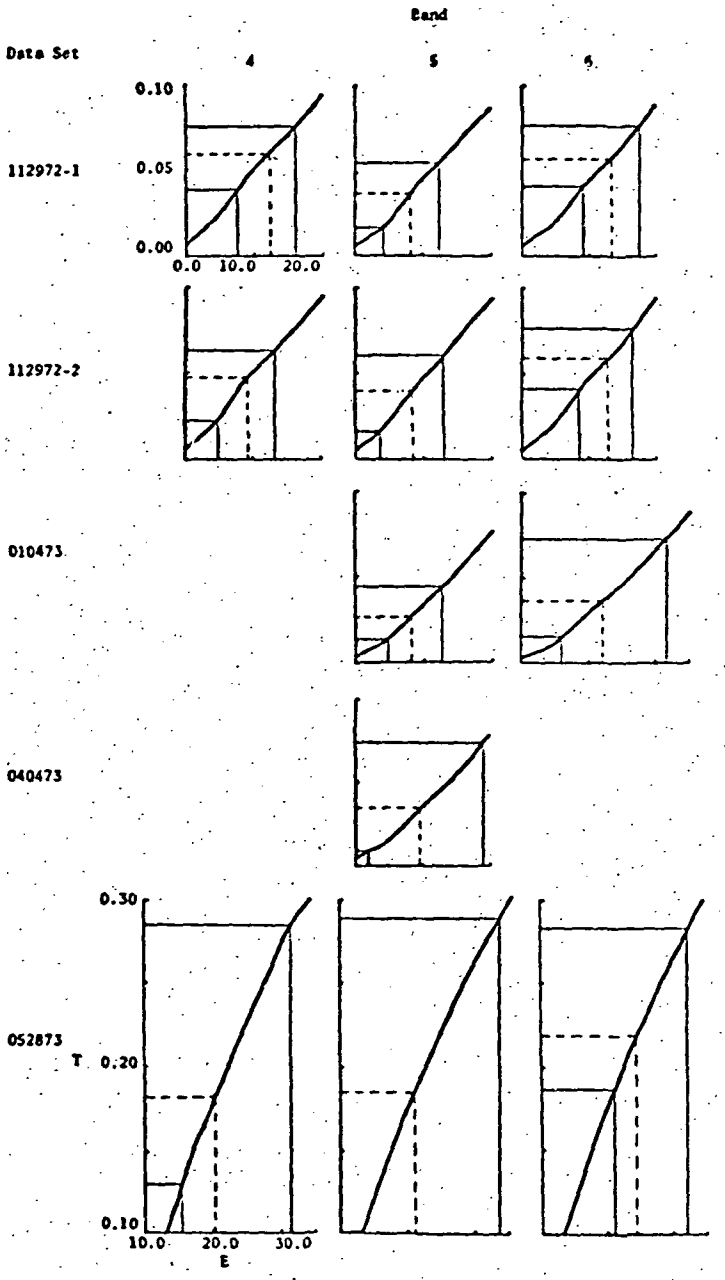

Fig. 31 ERTS MSS Imagery Sensitometry
Transmission versus Exposure

Signal-to-Noise of Scanned Data

In choosing the aperture sizes for scanning it is desirable to select as large an aperture as possible to minimize photographic granularity noise. However, one is limited in maximum aperture size by the microdensitometer capabilities and the desired resolution in the data. Therefore, there is always a finite, possibly negligibly small, amount of noise in the data.

To obtain a feeling for the noise in our data, curves of the standard deviation divided by the mean versus the mean, were plotted for step tablet (i.e. uniformly exposed areas) scans. These are shown in Figs. 32 and 33 in density units for the underflight images and transmission units for the ERTS images. The significance of these curves is based on the following reasoning.

Suppose a set of measurements are taken from a random process which has a Gaussian pdf with mean, M; and standard deviation σ:

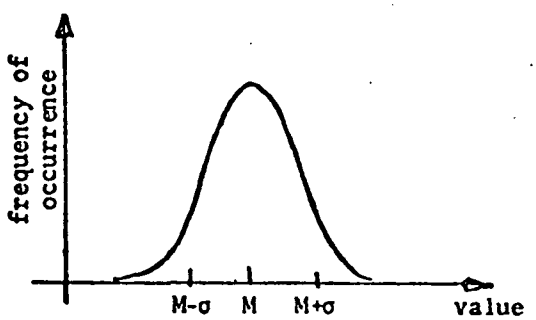

The desired value for the measurement is the mean and, for a Gaussian pdf, 68% of the values are within ±σ of the mean. The *percent error* for measurements in this range is thus,

$$\left|\epsilon_{rel}\right| \leq \left|\frac{M - M \pm \sigma}{M}\right| \leq \frac{\sigma}{M}$$

This is the quantity graphed in Figs. 32 and 33. The percent error of a single microdensitometer measurement will be less than or equal to these values in 68% of the measurements. Likewise, if the ordinate is doubled, the maximum percent error is given for 96% of the measurements.

Figure 32 indicates that the density noise in the underflight data is very small, owing to the large apertures used for these data. The transmission noise in the ERTS data (Fig. 33) is somewhat larger but remains generally less than 10%. The actual noise quantity of interest would be measured in exposure space. However, from the slopes of the calibration curves for these data, it can be seen that the exposure noise will usually be less than or approximately equal to the density or transmission noise (as defined above).

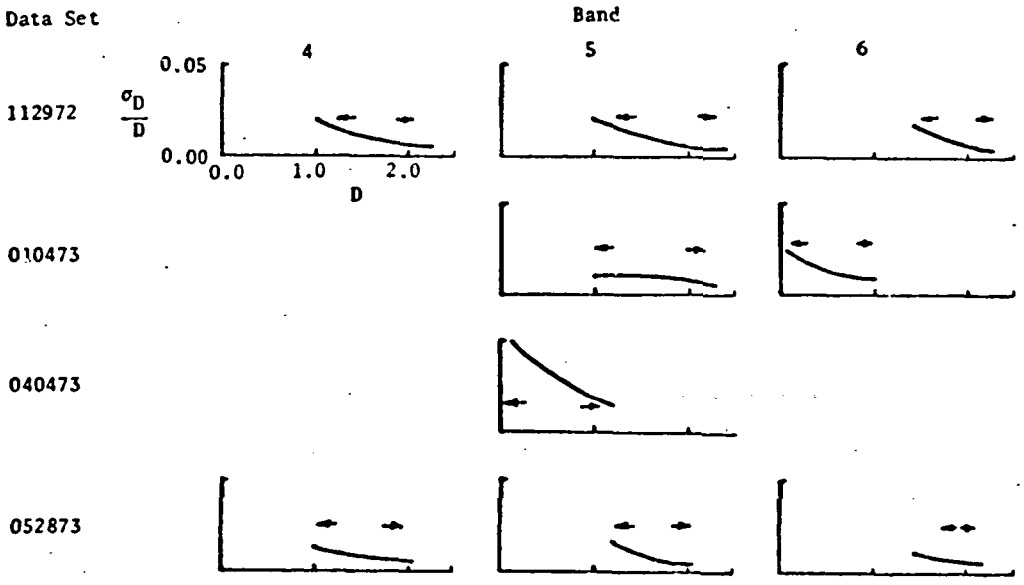

Fig. 32 Underflight Microdensitometer Data Noise (density units)

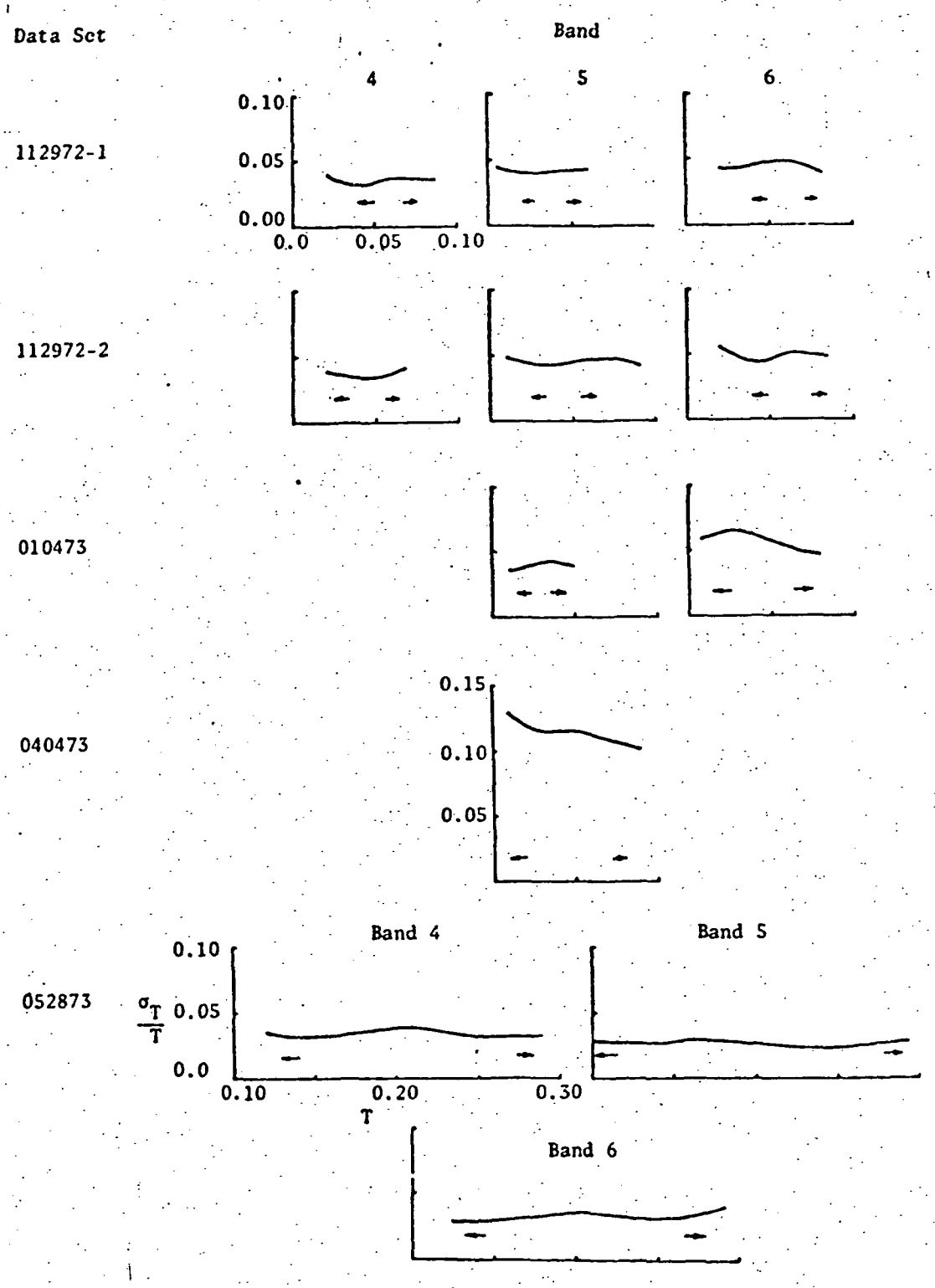

Fig. 33 ERTS MSS Microdensitometer Data Noise (transmission units)

APPENDIX B

Microdensitometer Parameters and Aperture OTF's

Summary of Microdensitometer Parameters

All data were taken on a Mann-Data Micro-Analyzer. Table 2 gives the aperture sizes and sample intervals used on all data in this report. Note that the ERTS imagery from 11/29/72 was scanned twice, with two different size slit apertures, to determine the sensitivity of the OTF analysis to choice of the slit length ratio (see Appendix E).

Table 3 gives the optical parameters of the microdensitometer. To minimize systematic differences between data and non-repeatability of focus setting, alignment, etc., the same optics were used in all cases (except data set 2 from 11/29/72). Figure 34 shows the optical configuration of the microdensitometer. The microspot setup was used on data set 040473 only.

The coherence of the illumination in the microdensitometer was not measured, but the choice of matching numerical apertures is the minimum requirement for incoherence to exist (Kinzley, 1972).

Scan Alignment

Proper alignment of the microdensitometer scans using ground reference points is usually very difficult, especially in the spacecraft imagery. The field of view in a microdensitometer is usually small and cannot be changed easily as with a photointerpreter's microscope. To assure proper alignment, pinholes were made in the imagery at the chosen ground reference points. Using a sharp knife or razor blade, holes of about 20-40 micrometers were produced. Centering accuracy of these holes is estimated to be 5-10 micrometers and is small compared to the slit lengths used.

TABLE 2

Microdensitometer Scan Parameters

Data Set	Underflight Imagery Aperture	Underflight Imagery Sample Int.	ERTS Imagery Aperture	ERTS Imagery Sample Int.	Remarks
112972-1	0.035 X 0.874	0.010	0.011 X 0.138	0.005	length ratio = 6.33
112972-2	0.035 X 0.874	0.010	0.009 X 0.107	0.005	length ratio = 8.17
010473	0.046 X 1.000	0.005	0.024 X 0.138	0.005	length ratio = 7.25
040473	0.093 X 0.093	0.020 - 0.040	0.011 X 0.011	0.010 - 0.010	Circular apertures x-y raster scans
061573	0.046 X 1.000	0.005	0.024 X 0.138	0.005	length ratio = 7.25

All dimensions in mm

TABLE 3

Microdensitometer Optical Parameters

	Manuf.	Focal length (mm)	NA	Remarks
influx optics (condenser)	B & L	40.	0.08	
efflux optics (objective)	B & L	48.	0.08	
	B & L	40.	0.08	(112972-2)

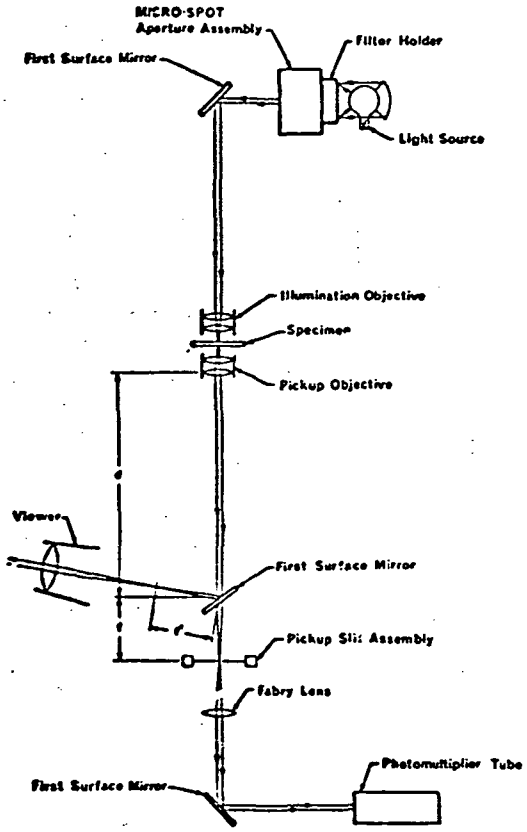

Micro-Spot Setup

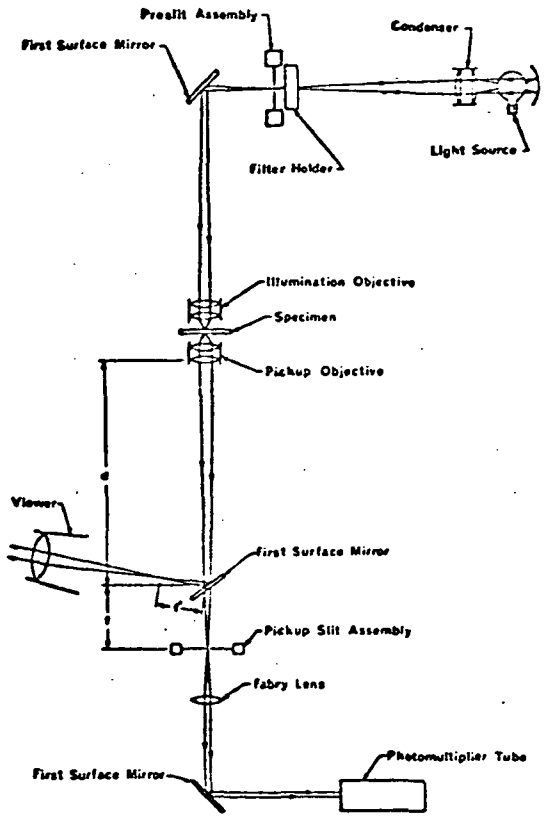

Slit Setup

Fig. 34 Optical Schematic of Mann-Data Microanalyzer
(Courtesy of Mead Technology Laboratories)

Aperture Transfer Functions

The sampled data from the microdensitometer are points off the convolution function of the scanning aperture with the photographic image. If the illumination at the sample is incoherent (see above), the aperture is described by its irradiance distribution and the film by its intensity transmission in the convolution process.

Because it was not possible to scale the slit *width* exactly between the underflight and ERTS-1 scans, the data must first be deconvolved, to obtain the true photographic image, before further analysis. The deconvolution is effected by:

1) density → transmission data conversion
2) Fourier transform of data
3) division of data spectrum by aperture OTF
4) inverse Fourier transformation of true data spectrum

The irradiance profile (line spread) of the microdensitometer aperture can be obtained by differentiating a scan of a perfect edge function (Tatian, 1965). For our data a partially transmitting metal edge was scanned each time the scan aperture was changed. Since direct differentiation (e.g. finite differences) amplifies noise, a combination smoothing and differentiating function (Lanczos, 1964) was used for these data.

The Fourier transform of the line spread function gives the optical transfer function (OTF) for the scan aperture. These are shown in Fig. 35 and are the functions used in step 3 above.

The aperture OTF correction must be applied at discrete sample intervals (given by 1/length of scan) in the frequency domain. Because image scans of

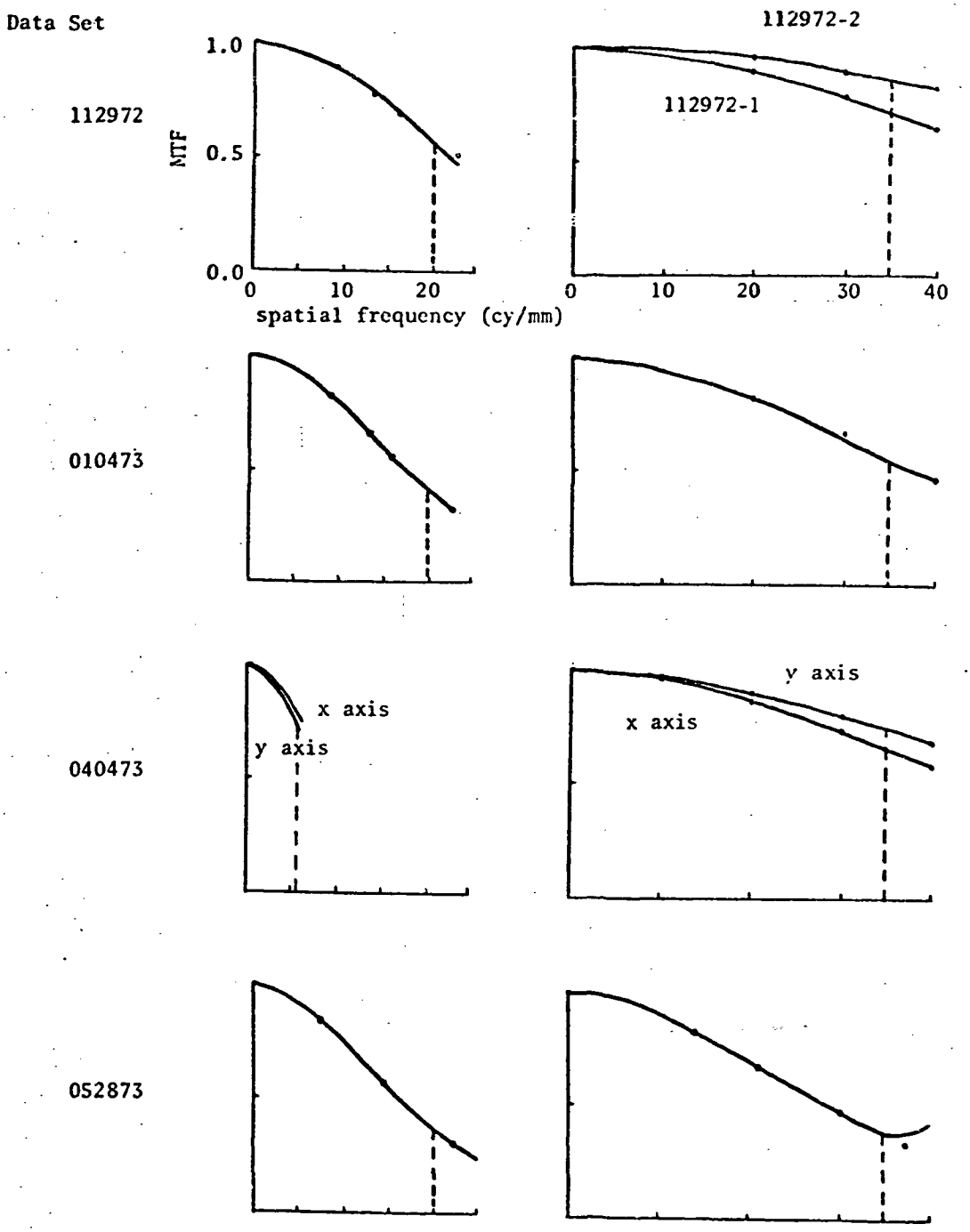

Fig.35 Microdensitometer Aperture OTF's

different lengths may have to be used in some cases, it is necessary to interpolate between sample points of either the image spectrum or the aperture OTF. Since the aperture OTF is typically a much smoother function, the interpolation was done on that data. It was found that power series polynomials gave a good approximation to the actual modulus and phase sample values of the OTF.

Note that the modulus is an even function of frequency so that only the even power coefficients of the polynomial approximations are significant. Similarly the phase is an odd function and thus only odd powers are used in the approximation. The approximating curves are therefore of the form:

modulus	$M(f) = 1 + Cf^2 + Ef^4$
phase	$P(f) = Bf + Df^3$

The two frequency values necessary to determine the two coefficients were chosen to give a good polynomial approximation over the entire frequency range of interpolation. The curves in Fig. 35 are those polynomials, with the actual sample points shown by dots. In all cases the P(f) was too small to be significant within the frequency range of interest (between zero frequency and the dashed lines in Fig. 35).

APPENDIX C

Line Spread Function Analysis of ERTS MSS

In order to obtain independent measurements of the ERTS MSS OTF to compare with those obtained using the scaling techniques described in this report, and to calculate an OTF for band 7, a suitable target, specifically a bridge, was selected in image number 1129-18181. The bridge is the San Mateo Bridge and is approximately 85 ft. wide and therefore is about 0.008 mm wide at the ERTS 70 mm scale. Thus it is negligibly small compared to the width of the spread function we wanted to measure. In addition, the bridge orientation was at an angle to the MSS scan direction which was nearly the same as the angle of the other scans made on this imagery.

The bridge was scanned with a slit-type aperture (0.011 x 0.275 mm) in a Joyce-Loebl Mk IIICS microdensitometer and the LSF calculated after deconvolution with the slit aperture and sensitometric conversion. It was not possible to use band 4 because of turbidity in the water around the bridge which reduced the contrast severely. Some turbidity in the other bands gave an elevated background level to the LSF, which was subtracted from the data, resulting in the curves in Fig. 36. The most notable feature of these LSF curves are the wings appearing around the LSF. It is believed that these are the result of the scan displacement anomaly (Colvocoresses and McEwen, 1973) and thus are a non-linear artifact in the LSF.

Now, because the other image scans were made of two-dimensional imagery, as opposed to the well-defined one-dimensional bridge, it was assumed that the wings appearing in LSF's obtained above would not be apparent in the LSF's obtained from the other image scans. Therefore a window function was applied to the bridge LSF's to eliminate the wings and give a more direct

comparison between the two sets of data. The resulting curves are shown in Fig. 37 along with the corresponding OTF's.

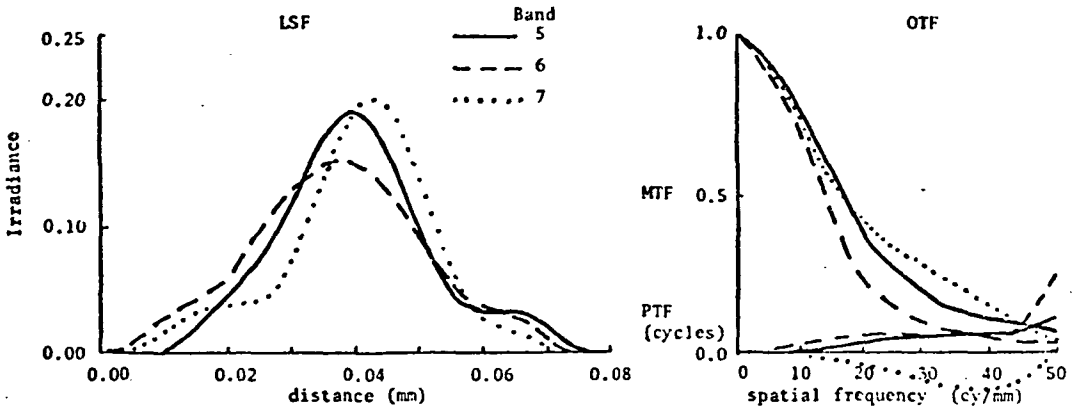

Fig. 36 ERTS MSS LSF's and OTF's from Bridge Scan

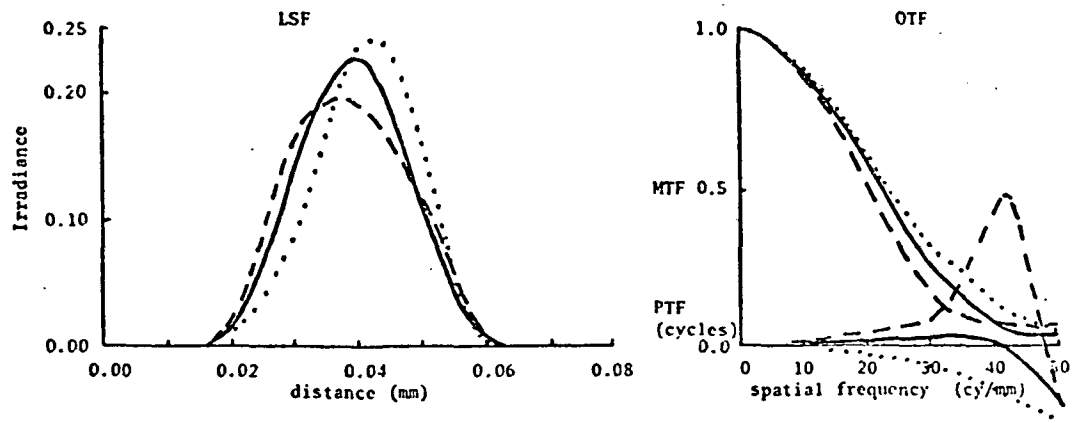

Fig. 37 ERTS MSS LSF's and OTF's from Bridge Scan after Appropriate Windowing of LSF's

Of course the choice of the particular window function to use above was somewhat arbitrary, and in any case does not represent a truly analytical correction for the scan anomaly. However the window chosen was the same as that used in the scaling procedures and thus gives a consistently obtained LSF for direct comparison.

APPENDIX D

Field Angle-Dependent Radiometric Correction for Underflight Imagery

The irradiance falloff across the image plane of an aerial camera system is a function of the field angle, ϕ, and for a simple lens, with no vignetting, obeys the relationship $\cos^4\phi$. Since, in the underflight imagery scans only, a large range of field angles is covered by the scan a correction must be made to the exposure values. The required correction is obtained by multiplying these exposure values by the factor $1/\cos^4\phi(P)$, where P is the image point of interest.[1] Since our scans are at an arbitrary angle and position within the format, the following process must be followed.

Given an arbitrary scan line in the image format, as shown below, image point positions are known, from the sample interval, as values of P, the

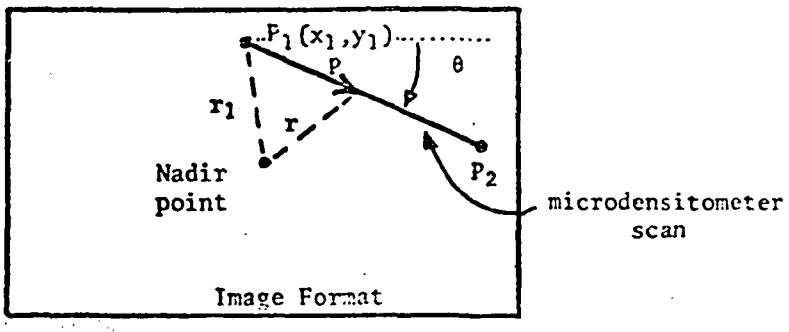

distance along line P_1P_2 from the point P_1. This distance then defines r, the radius from the nadir point to the position P in the image format:

$$r(P) = [P^2 + r_1^2 + 2P(x_1\cos\theta + y_1\sin\theta)]^{\frac{1}{2}}$$

[1] Since laboratory calibration for the irradiance falloff in the underflight Vinten cameras was not available, the $\cos^4\theta$ law was assumed to hold for all the imagery. This assumption is not unreasonable since the f-numbers used in the Vinten cameras were always greater than 9.5 thus reducing the possibility of vignetting.

Then, using the geometry for a simple optical system shown below,

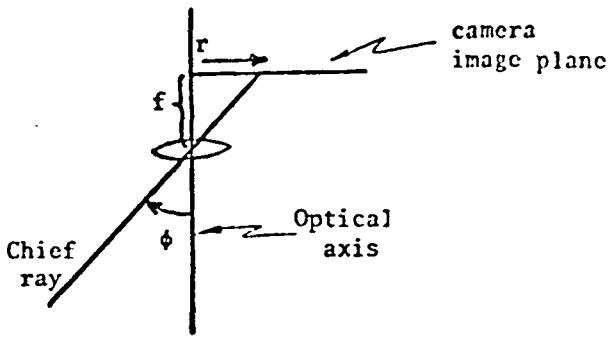

the field angle, ϕ, can be calculated using

$$\phi = \tan^{-1} \frac{r}{f}$$

where f is the known focal length of the camera system.

The variation for the required correction factor, $1/\cos^4\phi$, as a function of the image position along the microdensitometer scan line is shown in Fig.38 for the imagery obtained on 11/29/72 and 01/04/73. The position and orientations of these particular scans within the image format can be seen in Fig. 39.

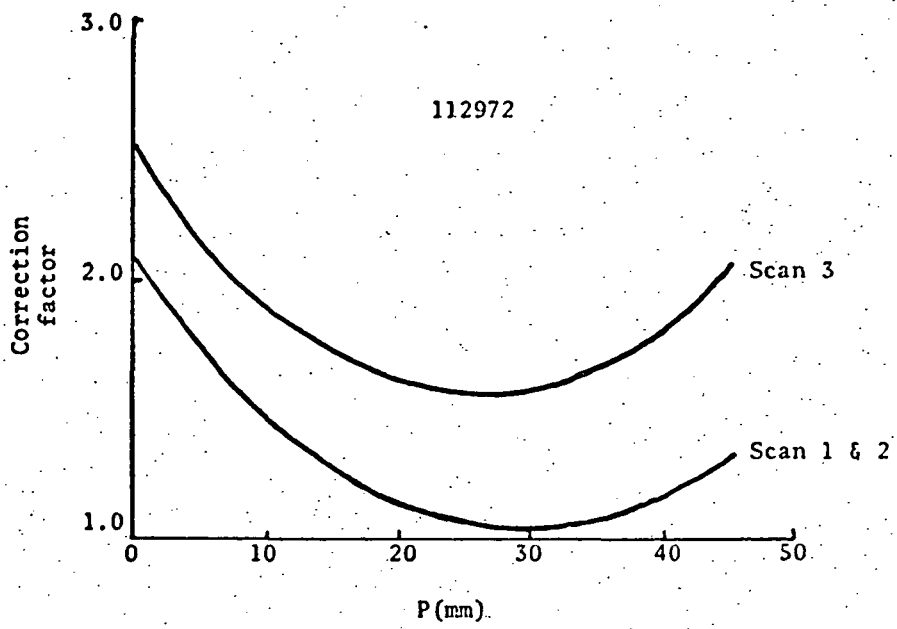

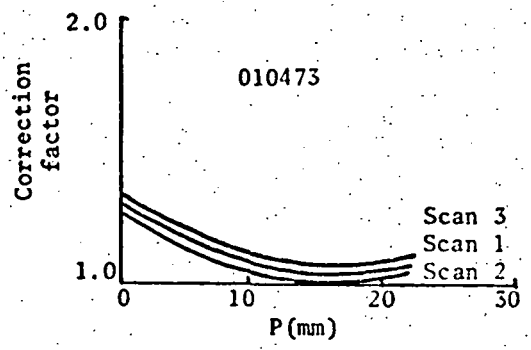

Fig. 38 Field angle radiometric correction factor for several scans

APPENDIX E

Details and Remarks on Digital Analysis

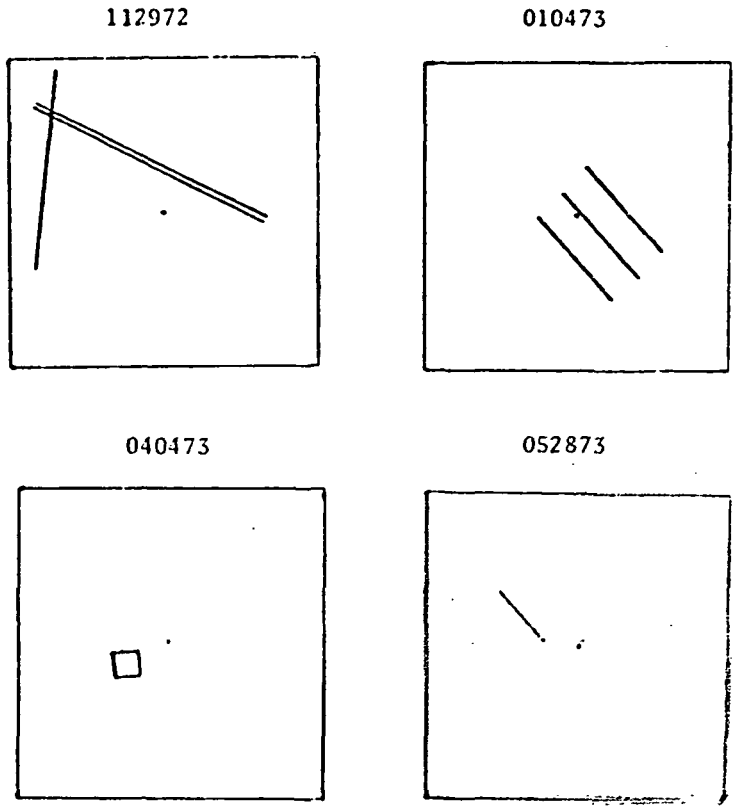

Fig. 39 Geometry of Microdensitometer Scans
Underflight Imagery

Correspondence Between 1-D and 2-D OTF Results

Out of the four dates of imagery analyzed for this report, only the imagery from 04/04/73 were scanned in two dimensions. Acquiring 2-D data allowed a comparison between the photographic product and the CCT image, which was already in 2-D sampled form. The question arises as to whether or not the results from the full 2-D analysis can be compared directly with the 1-D results, obtained for all other image dates.

It was decided to simulate the 1-D slit scans from the 2-D data by integrating sample points in one direction, over the length of a simulated slit reading. A pair of slits (one each for the U2 and ERTS images) with a length ratio of 7.0 was simulated and the scans were set up along the y direction of the imagery. From the 2-D arrays it was possible to obtain three effective 1-D slit scans. This data was then evaluated in the 1-D analysis program.

The results from the 1-D analysis are shown in Fig. 40 along with the profile of the 2-D OTF from the full 2-D analysis. Very good agreement is indicated between the two curves.

The above example simulated a choice of slit lengths giving a ratio very close to the exact scale between the images (equal to 7.04 from the 2-D scaling). Another set of simulated 1-D scans was set up with a length ratio of 7.6 and the analysis repeated. The result is shown in Fig. 41 and indicates low sensitivity in the OTF to the slit length ratio.

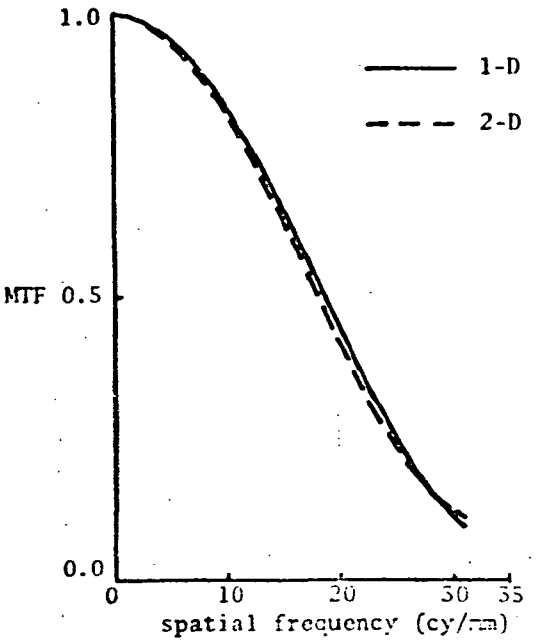

Fig.40 MTF Comparison between 1-D simulation and 2-D (slit scale = 7.0)

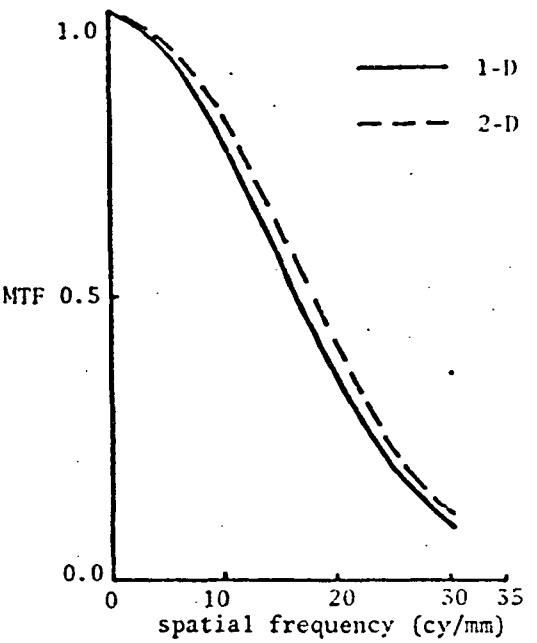

Fig. 41 MTF Comparison between 1-D simulation and 2-D (slit scale = 7.6)

Effect of Slit Length Ratio for 1-D Scans

The ERTS MSS imagery from 11/29/72 was scanned with two different slit apertures, one 0.011 x 0.138 mm and the other 0.009 x 0.107 mm. These two apertures had length ratios of 6.33 and 8.17 respectively with respect to the U2 aperture (0.035 x 0.874 mm), and bracketed the actual scale of about 7.1 between the images.

Two corresponding scan sections for each band are shown in Fig. 42. Since the two sets of microdensitometer data were taken on different dates there is the possibility of differences in scan alignment, in addition to expected differences caused by the change in scan apertures. Therefore, the differences between the curves in Fig. 42 cannot be separated into the two components, but their combined effects are evidently small. The MTF's calculated from these data are shown in Fig. 43 and indicate that the exact matching of slit length ratio to image scale ratio is not critical in OTF derivation.

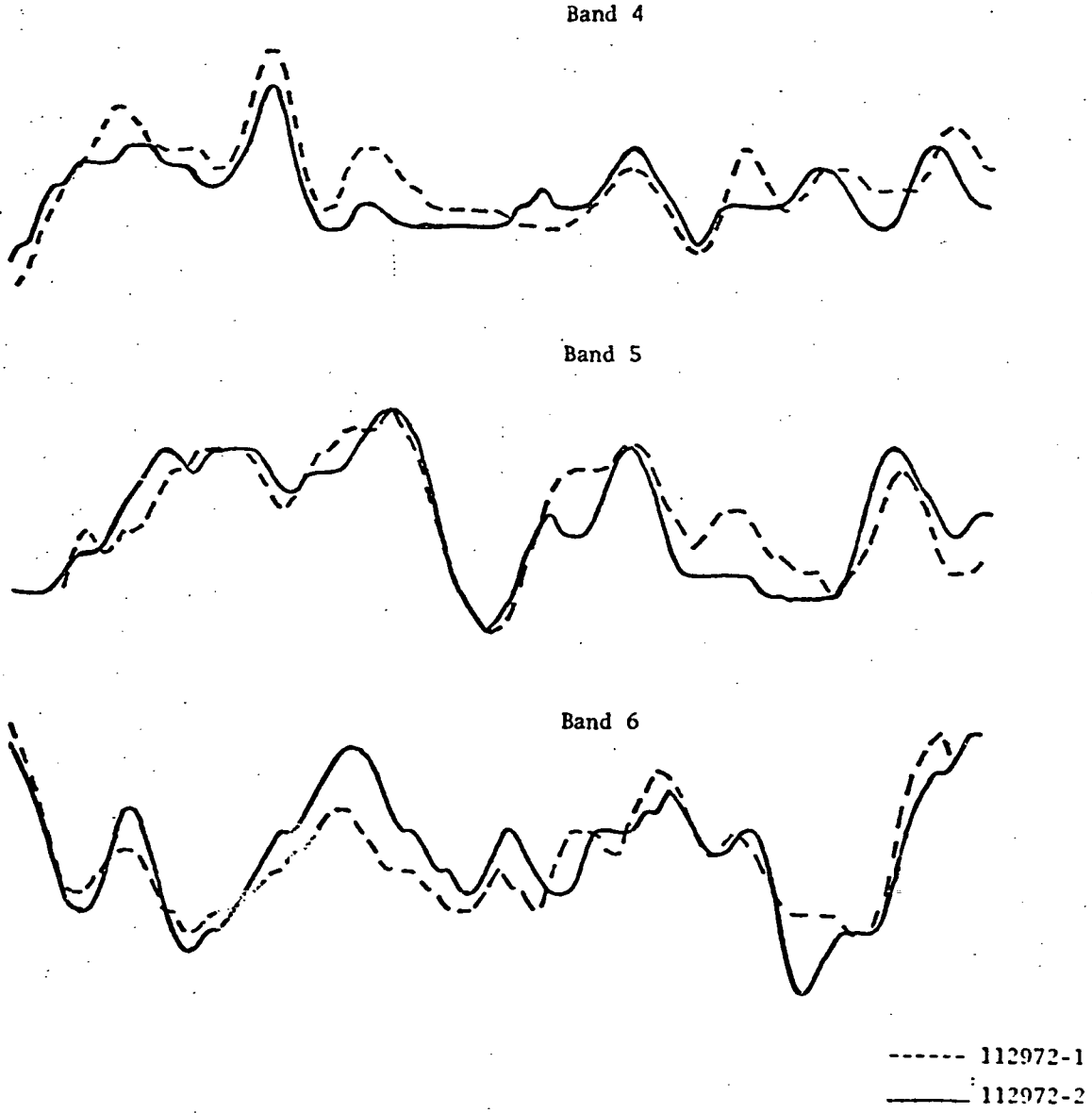

Fig. 42 Corresponding microdensitometer scans made with two different apertures

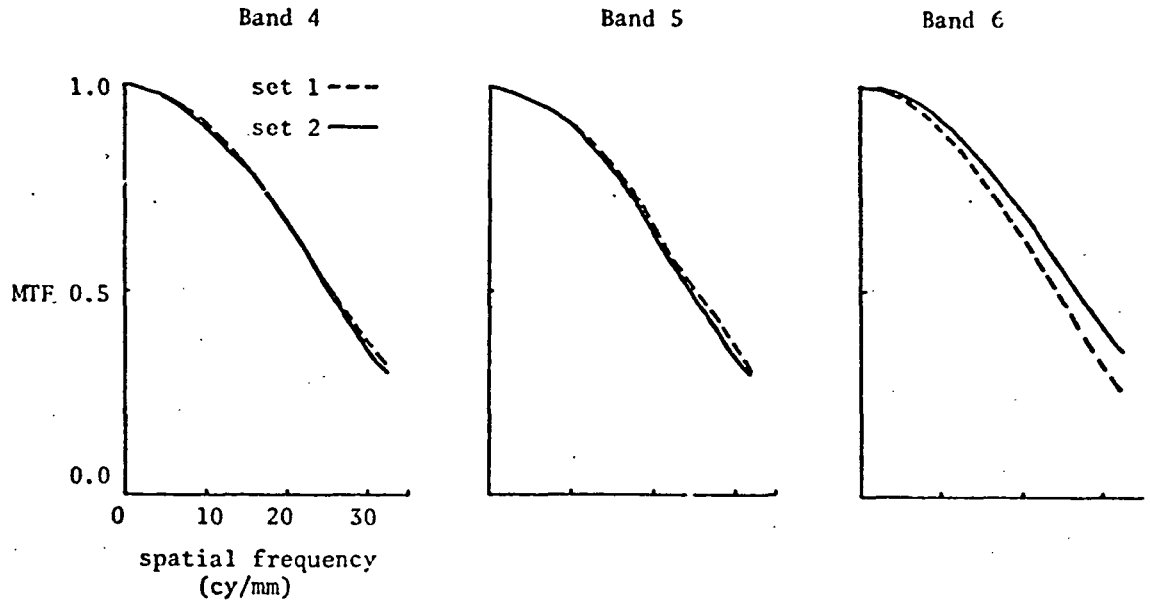

Fig. 43 MTF's obtained from scans made with two different apertures (112972)

Use of Fourier Interpolation for Scaling

When the two sets of imagery are scanned with a microdensitometer, the aperture length (i.e. the length perpendicular to the scan direction) is scaled as closely as possible to cover the same general ground area in the underflight and ERTS-1 images. Endpoints of the scans are determined by prominent ground features to insure the same ground coverage. However, the scan data are sampled and digitized when recorded. Thus when a section of this data is analyzed, the starting point in each image must be determined to be the same ground point (matching) and, since the sample intervals of the microdensitometer system cannot, in general, be changed by multiples of the exact scale between the images, one set of image data must be scaled in some way to correspond to the ground coverage of the other set of image data.

Since these operations must be performed in a discrete way (sampled data) it is necessary to have the same number of points in each set of data for comparison purposes. The scaling operation can be done in several ways, linear or polynomial interpolation being one (Schowengerdt and Slater, 1972). A technique with more theoretical validity was used for the 1-D OTF analysis. The approach is based on the following considerations. The spectrum of discrete data appears as below:

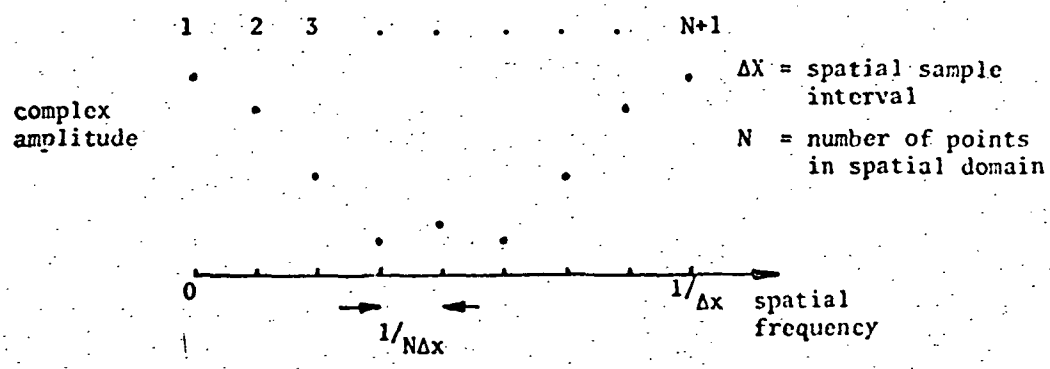

The spectrum is replicated at $1/\Delta x$ and sampled at $1/N\Delta x$. Suppose that N is increased by adding zeros between the replicated spectra:

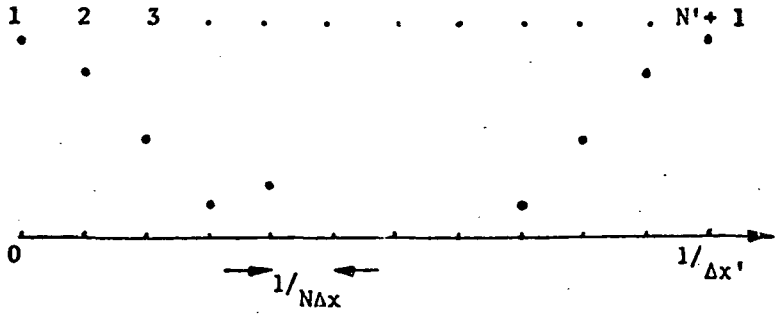

The sample interval in the frequency domain remains the same, but the sample interval in the spatial domain has effectively decreased,

$$\Delta x' = \frac{N}{N'}\Delta x$$

Since $N\Delta x$ has not changed, the same range of spatial data is sampled but at a smaller interval. Figure 44 illustrates the technique. A smooth function was sampled at 8 points and its discrete Fourier transform taken. Then 8 zeros were inserted into the spectrum as above, and the inverse transform calculated. The final data consists of the original 8 points with 8 interpolated points. The interpolation is of the sinc (x) = $\sin(\pi x)/\pi x$ type (Goodman, 1968, p. 25).

For image scaling, the underflight data has been scaled to match the ERTS-1 data, rather than visa versa, because the underflight scans, being made with a large aperture, are generally smoother and less disturbed by granularity than the ERTS-1 scans.

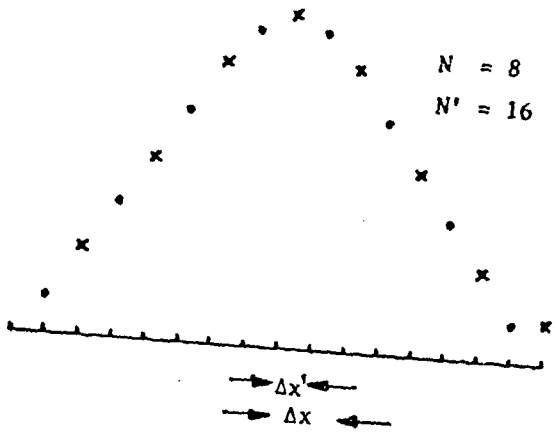

Fig. 44 Example of Fourier Interpolation

ERTS-1 MSS Detector Striping

One of the six detectors in each band of the MSS was calibrated incorrectly, resulting in the appearance of stripes in the imagery. This effect was observed in our studies in a pronounced way because of the nature of Fourier analysis. The striping represents a periodic structure, with a period of 6 x one detector width, superimposed on the imagery. Therefore the Fourier spectrum of the imagery should show a strong component at a spatial frequency equal to the reciprocal of that period. The particular numbers for 70 mm MSS imagery are,

Striping period = 6 x 0.023 = 0.138 mm

Frequency spike = 1/0.138 = 7.3 cycles/mm

Figure 45 shows microdensitometer scans of recorded Fourier spectra of an MSS image (see section III) along the azimuthal direction of the spikes (perpendicular to the MSS scan direction). These spectra show pronounced components at about 7 cycles/mm and additional higher order harmonics. Additional evidence of the striping is shown in Fig.46 where the unsmoothed y axis OTF for the CCT image of 04/04/73 is plotted. The spike at 7.5 cycles/mm indicates a frequency component in the image which is much stronger than the same component in the object.

These frequency domain curves suggest a possibly advantageous way to correct for the striping. Only two data points need to be corrected in the frequency domain to eliminate the fundamental component of the striping. With the computational speed advantages of the Fast Fourier Transform this correction may be economically better than a smoothing operation in the spatial domain.

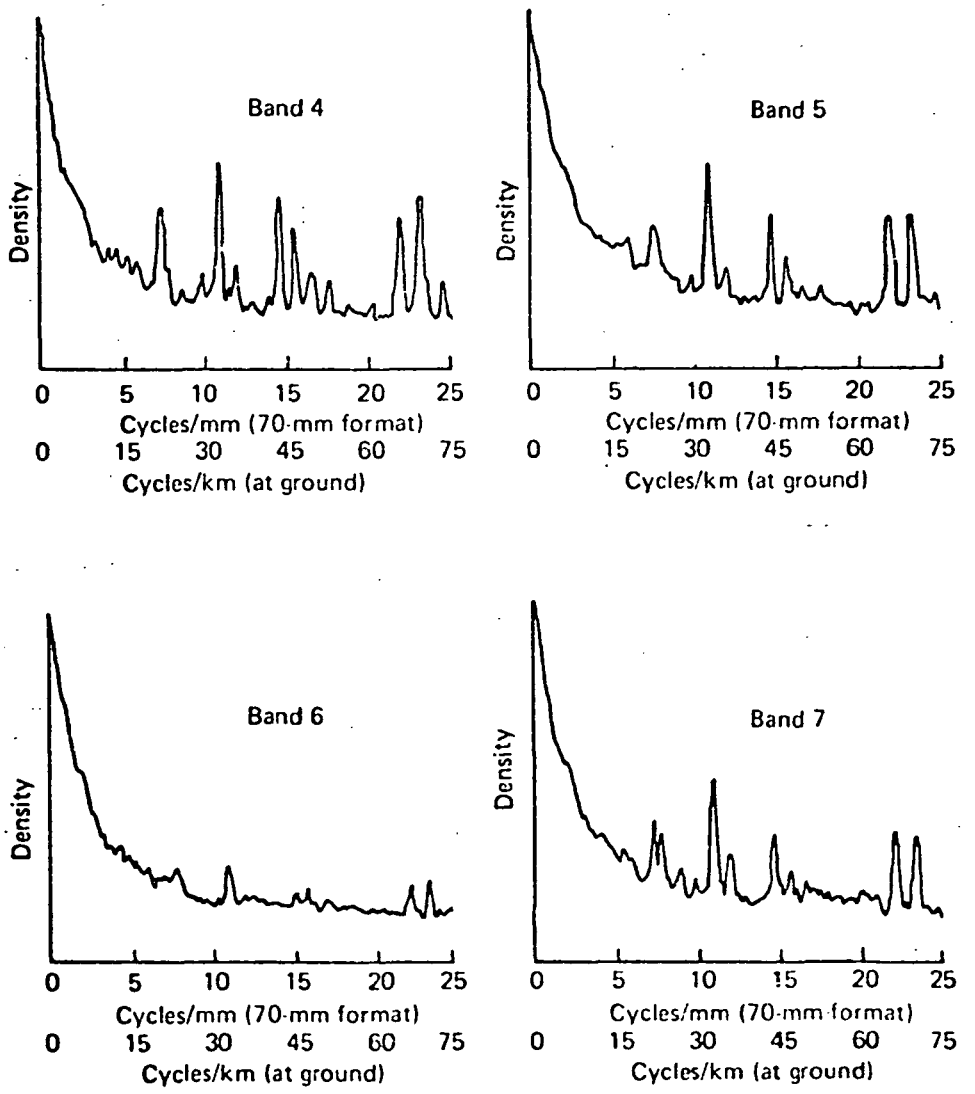

Fig. 45 Microdensitometer scans of photographically recorded Fourier spectra, indicating effects attributed to the ERTS scan lines.

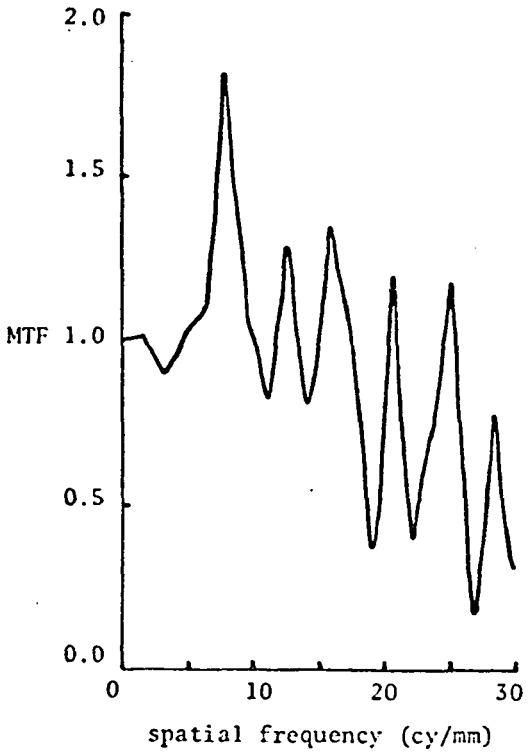

Fig. 46 Unsmoothed y-axis OTF for CCT image, 04/04/73, band 5

REFERENCES

G. D. Bergland, "A Guided Tour of the Fast Fourier Transform," IEEE Spectrum, 6, pp. 41-52, July 1969.

A. P. Colvocoresses, "Image Resolutions for ERTS, SKYLAB and GEMINI/APOLLO," Photogrammetric Engineering, 38 (1): 33-35, January 1972.

A. P. Colvocoresses and R. B. McEwen, "Progress in Cartography, EROS Program," *Symposium on Significant Results Obtained from Earth Resources Technology Satellite-1*, symposium held at Goddard Space Flight Center, March 5-9, 1973, NASA SP-327, Vol. I, Section B, p. 887-898.

S. C. Freden, "Introduction: Performance of Sensors and Systems," Earth Resources Technology Satellite-1 Symposium Proceedings, September 29, 1972.

J. W. Goodman, *Introduction to Fourier Optics*, McGraw-Hill 1968.

L. O. Hendeberg and E. Welander, "Experimental Transfer Characteristics of Image Motion and Air Conditions in Aerial Photography," Appl. Opt. 2(4):379-386, April 1963.

R. A. Jones and G. C. Trinks, "Near Field Diffraction in Contact Printing," Appl. Opt. 10 (7): 1659-1663, July 1971.

R. E. Kinzly, "Partially Coherent Imaging in a Microdensitometer," J. Opt. Soc. Am., 62 (3): 386-394, March 1972.

C. Lanczos , *Applied Analysis*, p. 321, Prentice Hall, Inc., Third printing, 1964.

E. H. Linfoot, *Fourier Methods in Optical Image Evaluation*, p. 31, Focal Press 1964.

P. G. Roetling, R. C. Haas, and R. E. Kinzly, "Some Practical Aspects of Measurement and Restoration of Motion-Degraded Images," *Evaluation of Motion-Degraded Images*, NASA SP-193, 1969.

R. A. Schowengerdt and P. N. Slater, "Determination of the In-Flight Optical Transfer Function of Orbital Earth Resources Sensors," Space Optics-Proceedings of the IX International Congress of the International Commission for Optics, National Academy of Sciences, 1974, Ed: B. J. Thompson and R. R. Shannon.

R. A. Schowengerdt and P. N. Slater, "Final Post-Flight Calibration Report on Apollo 9 Multiband Photography Experiment S065," NASA Contract NAS9-9333, Optical Sciences Technical Memorandum #3, May 1972.

R. M. Shaffer, "Film/Chemistry Selection for the Earth Resources Technology Satellite (ERTS) Ground Data Handling System," Image Technology, 15, p. 12, April/July 1973.

B. Tatian, "Method of Obtaining the Transfer Function from the Edge Response Function," J. Opt. Soc. Am., 55(8): 1014-1019, August 1965.

Acknowledgements

Ronald L. Antos gave much assistance in computer organization, checking, and analysis of the large amount of data generated during this project.

Mead Technology Laboratories, Dayton, Ohio, an Industrial Associate of the Optical Sciences Center, provided the microdensitometer scanning for this project. All scans were made on a Mann-Data Micro-Analyzer instrument.

Ames Research Center was very cooperative with this investigation in supplying simultaneous high-altitude imagery.